Theoretical and Applied Fracture Mechanics 106 (2020) 102489

Contents lists available at ScienceDirect

Theoretical and Applied Fracture Mechanics

journal homepage: www.elsevier.com/locate/tafmec

$C(t)$ dominance of the mixed I/II creep crack: Part II. Extensive creep

Yanwei Dai[a,*], Yinghua Liu[b,*], Fei Qin[a,*], Yuh J. Chao[c], Guian Qian[d]

[a] College of Mechanical Engineering and Applied Electronics Technology, Beijing University of Technology, Beijing 100124, China
[b] Department of Engineering Mechanics, AML, Tsinghua University, Beijing 100084, China
[c] University of South Carolina, 300 Main Street, Room A123, Columbia, SC 29208, USA
[d] State Key Laboratory of Nonlinear Mechanics (LNM), Institute of Mechanics, Chinese Academy of Sciences, Beijing 100190, China

ARTICLE INFO

Keywords:
Mixed I/II
Creep crack
C^*-integral
Constraint effect
Stress triaxiality

ABSTRACT

In the Part II of this paper, two typical specimens, i.e. compact tension shear (CTS) specimen and single edge notched (SEN) specimen, are selected as the numerical cases to analyse the dominance of C^*-integral for mixed I/II creep crack under extensive creep. C^*-integrals under different loading angles are presented with the same loading level for CTS specimens and SEN specimens. The equivalent creep zone enlarges with the decrease of the loading angle, which implies that the lower creep mixity occupies the larger equivalent creep zone under the same loading level. A normalized stress function method based on the FE calculation is given to obtain the distribution functions of mixed I/II creep crack tip fields. The comparisons of the FE solutions and HRR field are made for CTS and SEN specimens with various crack depths, and it can be found that the loss dominance of $C(t)$ becomes remarkable under those cases close to mode I loading. The Q-parameter computed with the tangential stress is found to be invalid to be used as the constraint parameter for mixed mode creep crack under the extensive creep regime because of the influence of blunting effect. The stress triaxiality along maximum tangential stress (MTS) direction is suitable to be selected as the constraint parameter for the mixed I/II creep crack tip field. The stress triaxiality is independent on the radial distance even in a wide range away from creep crack tip along the MTS direction.

1. Introduction

In the Part I of the paper, the asymptotic analysis for mixed I/II creep crack is presented under transient creep with boundary layer model [1]. According to Dai et al. [1], the stress field of creep crack may be different between transient creep and extensive creep due to accumulation of creep damage. Hence, it is necessary to investigate the mixed I/II creep crack tip field under extensive creep, i.e. the mixed I/II creep crack tip field dominated by C^*-integral.

Due to the potential influence of constraint effect on the fracture evaluation of flaw contained structures, characterizations of various modes of crack tip fields have drawn some concerns in recent investigations with different considerations [2–6]. For mixed I/II creep crack, it is suspected that there should be a transition between the mode I creep crack and mode II creep crack under mixed loading conditions [7–9]. Some results also demonstrated that there were some differences between mode I and mode II crack in various kinds of materials, e.g. Keiichiro and Hitoshi [10] presented that the mode I crack was initiated in a brittle manner, while mode II type crack initiation occurred in a ductile manner, and similar conclusions were given by Tvergaard [11]. The asymptotic field of mixed mode crack in plastic materials under plane stress condition was studied by Stepanova and Yakovleva [12] with perturbation theory method which provides a novel insight in this area. The finite deformation [13] was considered to be important on the near crack tip field of the power-law elastoplastic material. However, the influence of finite deformation on the mixed mode creep crack under extensive creep regime is unclear.

In fact, there are some typical test specimens which have been adopted to study mixed I/II crack tip field, e.g. Richard and Benitz [14] proposed a mixed mode test device which was described as compact tension shear (CTS) specimen, though there is no standard industry tested specimen for the mixed I/II creep crack. Aoki et al. [15] took an experimental investigation on aluminum alloy with a CTS specimen containing mixed mode crack, and they found that the crack tip under pure mode II case presents sharpening effect. Ayatollahi et al. [16] proposed a single edge notched (SEN) specimen under mixed loading, and the biaxiality of the SEN specimen under different loading angles were discussed. The four-point bending (FPB) specimen was adopted by Maccagno and Knott [17] to test the mixed mode type crack. The Arcan type specimen is also widely used to study the mixed mode fracture for

* Corresponding authors.
E-mail addresses: ywdai@bjut.edu.cn (Y. Dai), yhliu@mail.tsinghua.edu.cn (Y. Liu), qfei@bjut.edu.cn (F. Qin).

https://doi.org/10.1016/j.tafmec.2020.102489
Received 26 June 2019; Received in revised form 9 January 2020; Accepted 10 January 2020
Available online 12 January 2020
0167-8442/

both linear elastic material [18] and elastoplastic material [19,20]. Ayatollahi and coworkers [21,22] presented a semi-circular bend (SCB) specimen to test the mode II and mixed mode crack tip field. There are also some other specimens e.g. inclined cracked specimen [23] and diagonally loaded square plate (DLSP) specimen [24]. Although different specimens have been proposed, CTS and SEN specimens under mixed mode loadings may be the most typically adopted specimens for mixed I/II crack investigations.

Under creep regime, Brockenbrough et al. [25] took the mixed I/II creep crack test in a circular plate and found the creep zone of mode II crack grows faster than mode I crack. Hyde and Chamber [26] performed an experimental investigation for a mixed mode creep crack, and the C^*-integral was used and it was found that the prediction is quite reasonable with a modification. Poquillon et al. [27] also presented an experimental test on the mode II creep crack, and the sharpening effect was verified. Gordon and McDowell [28] carried out a finite element (FE) study on the interface creep crack between graded materials and found that the creep strain grew faster under shearing mode. Some recent advances on studies of mixed mode creep crack were reported by Dai et al. [1,9], Kumar et al. [29] and Zhao and Nikbin [30], which indicates that the investigations of mixed mode creep crack have recently drawn a lot attentions.

In those available literatures, there are no available articles to discuss the $C(t)$ dominance or C^* dominance for the mixed I/II creep crack under the extensive creep range as far as the authors' knowledge. The constraint effect for the extensive mixed I/II creep crack is also not studied yet. Furthermore, the extensive creep crack tip field is rather different comparing with that of transient creep crack tip field which implies that the mixed mode crack tip field under extensive creep is necessary to be studied.

The current work is aimed to quantify the C^* dominance for the mixed mode creep crack under extensive creep condition. Only the plane strain condition is focused in this part of the paper. Compact tension shearing (CTS) specimens and single edged notch (SEN) specimens under mixed loading conditions are adopted to perform the analysis in this part of the paper. In order to investigate the dominance of $C(t)$ or C^*-integral, two crack lengths, i.e. shallow crack with $a/W = 0.1$ and deep crack with $a/W = 0.5$, for both CTS specimen and SEN specimen are analysed. The structure of the paper is organized as follows. The theoretical background is presented in Section 2. The finite element (FE) model and numerical procedures are given in Section 3. The results and discussions are shown in Section 4. In the end, the conclusions are drawn in the last section.

2. Fracture framework of mixed mode creep crack under extensive creep range

The power-law creep equation is adopted and presented as [31]

$$\dot{\varepsilon} = \frac{\dot{\sigma}}{E} + \dot{\varepsilon}_0\left(\frac{\sigma}{\sigma_0}\right)^n \tag{1}$$

where E, n, $\dot{\varepsilon}_0$, σ_0, and $\dot{\sigma}$ are Young's modulus, creep exponent, reference creep strain rate, reference stress and stress with rate form, respectively. The creep coefficient is calculated as $A = \dot{\varepsilon}_0/\sigma_0^n$.

For the mixed I/II creep crack tip field under the extensive creep, the stress, strain and displacement components should be presented as [25]

$$\sigma_{ij} = \sigma_0\left(\frac{C^*}{\dot{\varepsilon}_0\sigma_0 I_n r}\right)^{1/(n+1)}\tilde{\sigma}_{ij}(\theta, n, M^c) \tag{2}$$

$$\dot{\varepsilon}_{ij} = \dot{\varepsilon}_0\left(\frac{C^*}{\dot{\varepsilon}_0\sigma_0 I_n r}\right)^{\frac{n}{n+1}}\tilde{\varepsilon}_{ij}(\theta, n, M^c) \tag{3}$$

$$\dot{u}_i = \dot{\varepsilon}_0 r\left(\frac{C^*}{\dot{\varepsilon}_0\sigma_0 I_n r}\right)^{\frac{n}{n+1}}\tilde{u}_i(\theta, n, M^c) \tag{4}$$

in which I_n is the integral constant which is traditionally considered to be dependent on power-law exponent n and mixity factor M^c as well as crack front stress state. $\tilde{\sigma}_{ij}$, $\tilde{\varepsilon}_{ij}$ and $\tilde{u}_i$ are the dimensionless angular stress function, dimensionless angular strain function and dimensionless displacement component, respectively. Herein, the mixity factor parameter is presented as follows.

$$M^c = \frac{2}{\pi}\left|\arctan\left(\frac{\tilde{\sigma}_{\theta\theta}(\theta=0)}{\tilde{\sigma}_{r\theta}(\theta=0)}\right)\right| \tag{5}$$

where $\tilde{\sigma}_{\theta\theta}$ and $\tilde{\sigma}_{r\theta}$ are the dimensionless normalized tangential stress and shearing stress component, respectively. This definition is always used to characterize creep mixity factor if the asymptotic solutions of the first order term are computed [9].

The formula to present the C^*-integral in Eqs. (2)–(4) should be written as below [32]

$$C^* = \int_\Gamma\left[W^*\mathrm{d}y - T_i\frac{\partial\dot{u}_i}{\partial x}\mathrm{d}x\right] \tag{6}$$

where W^*, T_i, $\dot{u}_i$, $\mathrm{d}y$ and $\mathrm{d}x$ are the strain energy rate density, traction force along the integral contour, displacement rate, increment of y-direction and increment of x-direction, respectively. The definitions of the above parameters are presented in Fig. 1. The difference between $C(t)$-integral given in the Part I and C^*-integral in Eq. (6) is that C^*-integral presents the path-independency under extensive creep.

C^*-integral can be presented as a function of so-called creep stress intensity factor under mixed I/II creep crack which is presented as below [3,4,33]:

$$C^* = (K^{cr})^{n+1}\dot{\varepsilon}_0\sigma_0 I_n(n, M^c) \tag{7}$$

where the creep stress intensity factor K^{cr} is given as

$$K^{cr} = \left(\frac{C^*}{\dot{\varepsilon}_0\sigma_0 I_n}\right)^{1/(n+1)} \tag{8}$$

It should be mentioned that Eq. (8) is as same as the creep intensity factor defined by Shlyannikov et al. [33] which is used under mode I case.

3. Finite element model and numerical procedures

To validate the results, the finite element (FE) code ABAQUS [34] is adopted to perform the analyses. Two typical specimens, i.e. single edge notched (SEN) specimen and compact tension shear (CTS) specimen, are adopted in the analyses. The detailed configurations for SEN specimen and CTS specimen are shown in Fig. 2. To overcome the difficulty of loading, a perfect connection fixture is adopted which is as same as that given by Ayatollahi et al. [16].

The width and height for CTS specimen are 50 mm and 60 mm, respectively. The ratios of a/W for CTS specimen take 0.1 and 0.5, respectively. In order to describe the loading angle between the loading direction and the crack front, a loading angle β is defined in Fig. 2. For

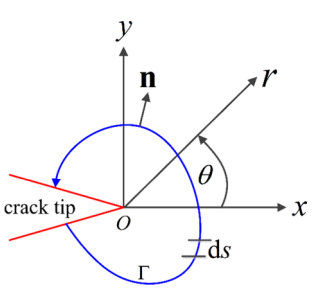

Fig. 1. Configuration of the coordinate used in the calculations.

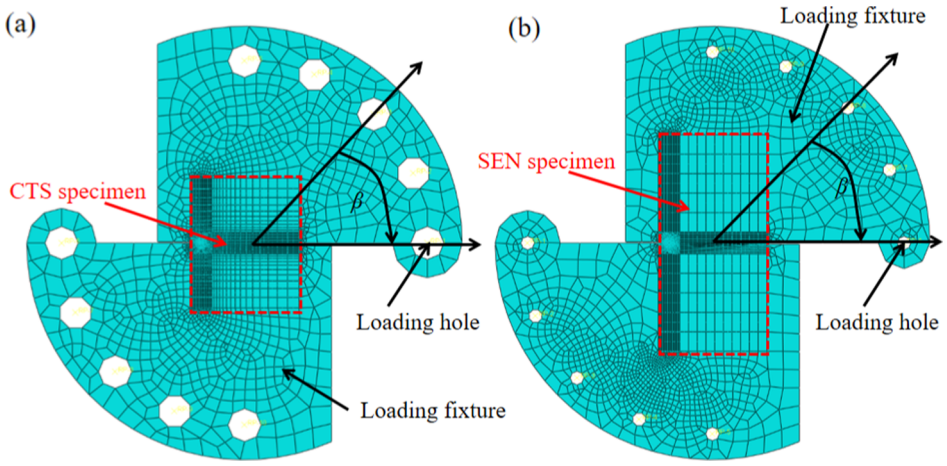

Fig. 2. Specimen configurations of (a) CTS specimen and (b) SEN specimen.

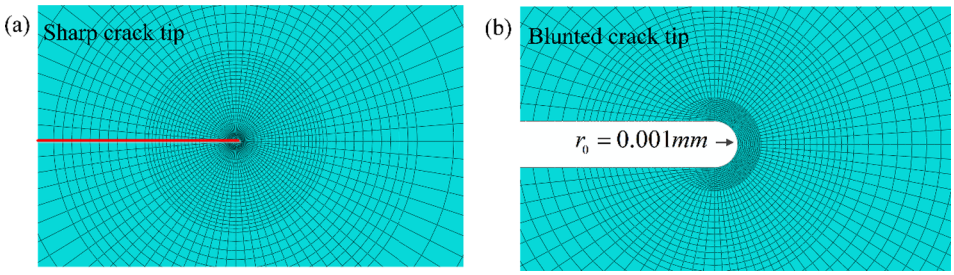

Fig. 3. FE meshes for (a) sharp crack tip and (b) blunted crack tip.

the CTS specimens, the loading angles adopt 0°, 22.5°, 45°, 67.5° and 90°, respectively. The loading level is kept as 1 kN during the whole calculations. The crack tip element is singular element which can be seen in Fig. 3(a). The element type used here is the same as the boundary layer formulation presented in the Part I of this paper, i.e. eight nodes plane strain element with integration reduction (CPE8R). The total element number varies between 5957 and 6433. The element type is kept as the same regardless of specimen type.

The loading levels for these different loading angles are kept as 1 kN for SEN specimens, i.e. $a/W = 0.5$, and shallow SEN specimen, i.e. $a/W = 0.1$. The loading angle β for the SEN specimen is defined as the same as that in CTS specimen. The width and height of the SEN specimen are 60 mm and 120 mm, respectively. The element number for SEN specimen varies from 3339 to 3959.

For creep crack, the blunting effect was found to be important on the influence of the creep crack tip field [1,35]. To investigate the blunting effect for the mixed mode type creep crack, the blunted type creep crack is presented with a notch tip radius 0.001 mm (see Fig. 3(b)). Except for the difference of crack, the geometry dimension and loading level for the blunted models are kept as the same as those of the sharp cracked specimens.

The material properties used in calculations are given as follows. Young's modulus E, reference stress σ_0 and Poisson's ratio ν are kept as 125 GPa, 180 MPa and 0.3, respectively. The creep coefficient in Eq. (1) is adopted as 3.20×10^{-11} MPa^{-n} h^{-1} and creep exponent n is idetical to 3, respectively. The material properties used here are close to type 1/2CrMoV [36] around 550 ℃ in engineering practices.

4. Results and discussions

4.1. C*-integral and creep zone comparisons

4.1.1. C*-integral

The C^*-integral is obtained from the in-built domain integral of ABAQUS itself. The contour integral method is robust enough which has been demonstrated by Kim et al. [37]. Herein, the $C(t)$-integral is determined by averaging values of ten integral contours around the crack tip. The $C(t)$-integral becomes C^*-integral if it presents to be path-independency. For the CTS specimen, the variations of $C(t)$-integral under different loading angles are given in Fig. 4. As presented in the Part I of the paper, the $C(t)$-integral under transient creep can be expressed as:

$$C(t) = \frac{(1-\nu^2)K_{\text{eff}}^2}{(n+1)Et} \tag{9}$$

where K_{eff} is the effective stress intensity factor (SIF) which is calculated as $K_{\text{eff}} = \sqrt{K_{\text{I}}^2 + K_{\text{II}}^2}$ and t is the creep time. Herein, K_{I} and K_{II} are SIF of mode I and mode II, respectively. From Eq. (9), the level of $C(t)$ under transient creep is determined by the level of K_{eff}. The transition time is defined as below for mixed I/II condition.

$$t_{\text{T}} = \frac{(1-\nu^2)K_{\text{eff}}^2}{(n+1)EC^*} \tag{10}$$

in which ν and E are Poisson's ratio and Young's modulus, respectively. The redistribution time t_{red} is defined as $(n+1)t_{\text{T}}$.

K_{eff}, C^*-integral and transition time t_{T} for CTS specimens and SEN specimens computed in this paper are given in Tables 1–4. For the condition with loading angle 0°, the value of K_{I} is much less than K_{II}, hence, it's considered to be pure II case for both CTS and SEN specimens. For loading angle 90°, the value of K_{II} is much less than K_{I}, hence, it is reasonably considered to be pure mode I case. The K_{eff} increases with the rise of the loading angle for all the calculated cases.

It can be seen that C^* of deep cracked CTS specimen presents the larger value than that of shallow cracked CTS specimen. The transition time increases with the rise of loading level. Transition time of the mode I case is larger than that of mode II. It reveals that the accumulation of creep strain under mode II case is faster than that of mode I condition. The C^*-level decreases with the increase of loading though

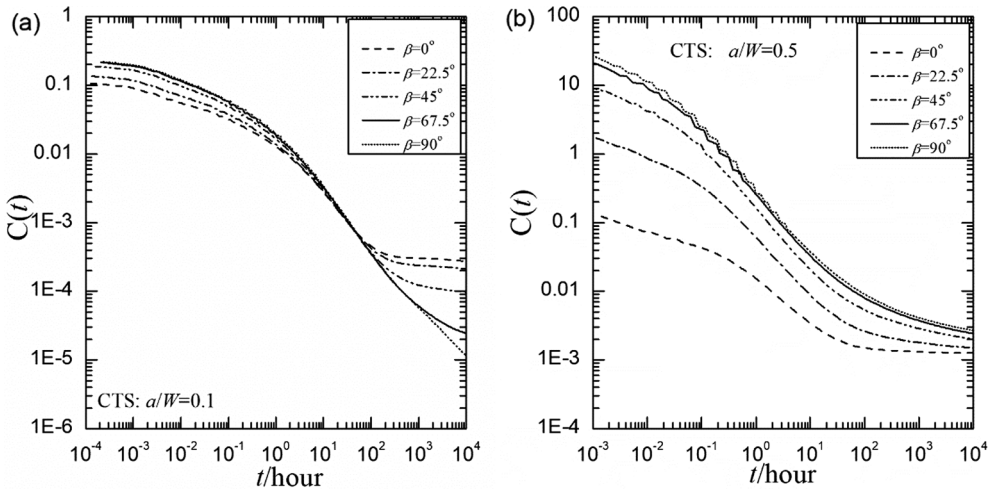

Fig. 4. Variations of $C(t)$ with creep time under different loading angles for CTS specimen with (a) $a/W = 0.1$ and (b) $a/W = 0.5$.

the K_{eff} increases with the rise of the loading for the shallow cracked CTS specimen. For deep cracked CTS specimen, mode I condition possesses the lowest C^* level than those of other specimens while the mode II CTS specimen has the highest C^* level. Similar conclusions can be obtained for the SEN specimens.

The variations of $C(t)$-integral with creep time for the CTS specimens and the SEN specimens are presented in Figs. 4 and 5, respectively. The tendencies of $C(t)$-integral for SEN specimens are quite similar to those of CTS specimens. It can be seen that the values of C^*-integral under small loading angle are higher than those of large loading angles for shallow cracked specimens. However, the C^*-integrals under small loading angles are smaller than those of large loading angles for deep cracked specimens. It reveals that the loss dominance of C^* enlarges with the increase of loading angle.

In fact, Ainsworth and Budden [38] proposed a relationship to describe the variation of $C(t)/C^*$ with normalized creep time $\tau = t/t_{red}$ which is presented as below.

$$\frac{C(t)}{C^*} = \frac{(1+\tau)^{n+1}}{(1+\tau)^{n+1}-1} \tag{11}$$

where n is the creep exponent. Kim et al. [37] presented a relation with the following form.

$$\frac{C(t)}{C^*} = \frac{(1+\tau)^{4.5}}{(1+\tau)^{4.5}-1} \tag{12}$$

Note that both equations are originally proposed for the mode I creep crack in those investigations.

Some numerical works [37,38] have demonstrated that Eqs. (11)-(12) are quite reasonable for mode I creep crack. Herein, the comparisons for CTS specimens and SEN specimens between the FE results and results calculated with Eqs. (11)-(12) are made in Figs. 6 and 7, respectively. It can be found that solutions obtained based on Eq. (11) and Eq. (12) are close to those FE solutions for shallow cracked CTS and SEN specimens, which implies that Eqs. (11)–(12) are valid for shallow mixed I/II crack of CTS and SEN specimens. However, the agreement between Eqs. (11)–(12) and FE results deviates slightly for deep cracked CTS and SEN specimens, and the FE results are a litter higher than solutions computed with Eqs. (11)–(12). Generally, Eqs. (11) and (12) can be extended to mixed I/II creep conditions based on the computations performed here.

4.1.2. Equivalent creep strain evolutions

To present the evolution characteristics of creep crack tip under different loading angles for various specimens, the equivalent creep zones of CTS specimens and SEN specimens are presented in Figs. 8 and 9, respectively. Herein, the equivalent creep zone is defined as the enclosed area with the same isoline under the same value of equivalent creep strain. The evolutions of equivalent creep strain can reflect the evolutions of creep crack tip to some extent. It should be noted that the solutions are directly extracted from ABAQUS. These results are kept under the same isoline with equivalent creep strain of 0.05 for CTS specimens and SEN specimens. It should be mentioned that the loading levels for these specimens are kept to be the same. Note that different loading angles represent different creep mixity factors, i.e. $\beta = 0^\circ$ represents mode II case, $\beta = 90^\circ$ represents mode I case and the other loading angles are intermediate modes between mode I and mode II, i.e. mixed I/II mode.

For the equivalent creep zone of CTS specimens shown in Fig. 8, the mode II case ($\beta = 0^\circ$) contains the largest region comparing with other conditions. It reveals again that the evolution of equivalent creep zone under mode II case is faster than the mode I case. Furthermore, the creep region increases with the decrease of loading angle, i.e. the creep region decreases with the improvement of creep mixity factor. The shape of mode II creep crack presents the “fish tail” shape. In fact, the creep region with isoline of 0.05 under mode II case includes the ligament length of the creep crack front for deep cracked specimens.

It can be found that the equivalent creep zone under $\beta = 0^\circ$ presents the largest equivalent creep zone size, and the loading angle at $\beta = 90^\circ$ dominates the smallest equivalent creep zone. The occurrence of mixed mode type creep crack grows faster than that of pure mode I case. The evolutions of equivalent creep zone with creep time under various creep

Table 1
Fracture parameters for different loading angles of specimen with $a/W = 0.1$.

β	K_I (MPa·mm$^{1/2}$)	K_{II} (MPa·mm$^{1/2}$)	K_{eff} (MPa·mm$^{1/2}$)	C^*(MPa·mm/h)	t_{red} (h)	t_T (h)
0	0.1112	98.88	98.88	2.72E−04	261.40	65.35
22.5	61.51	92.81	111.34	2.12E−04	425.94	106.49
45	111.4	69.43	131.27	9.74E−05	1287.86	321.97
67.5	148.6	37.93	153.36	2.45E−05	6982.21	1745.55
90	160.7	0.6256	160.70	1.16E−05	16202.03	4050.51

Table 2
Fracture parameters for different loading angles of CTS specimen with $a/W = 0.5$.

β	K_I (MPa·mm$^{1/2}$)	K_{II} (MPa·mm$^{1/2}$)	K_{eff} (MPa·mm$^{1/2}$)	C^* (MPa·mm/h)	t_{red} (h)	t_T (h)
0	3.207	71.25	71.32	1.26E−03	29.43	7.36
22.5	168.2	66.59	180.90	1.50E−03	158.48	39.62
45	307.7	51.81	312.03	2.02E−03	351.38	87.85
67.5	400.13	29.14	401.19	2.43E−03	482.29	120.57
90	431.9	2.02	431.90	2.70E−03	503.19	125.80

Table 4
Fracture parameters for different loading angles of SEN specimen with $a/W = 0.5$.

β	K_I (MPa·mm$^{1/2}$)	K_{II} (MPa·mm$^{1/2}$)	K_{eff} (MPa·mm$^{1/2}$)	C^* (MPa·mm/h)	t_{red} (h)	t_T (h)
0	3.073	78.04	78.10	1.601E−3	27.72	6.93
22.5	176.5	73.69	191.27	2.319E−3	114.86	28.72
45	323.0	57.32	328.05	3.880E−3	206.08	51.52
67.5	416.1	31.89	417.32	5.142E−3	246.19	61.55
90	449.1	2.182	449.11	5.610E−3	261.73	65.43

mixity factors are given in Appendix A. Similar tendencies can be found for mixed mode creep crack at various creep time. The variations of equal equivalent stress with creep time are also presented in Appendix A.

4.2. CTS specimen

The characterizations of crack tip stress field for the CTS specimen under different loading angles are a preliminary to understand the crack tip field of the CTS specimen. Herein, the angular and radial distribution of the stress component are presented firstly. Then the relations between the elastic mixity factor creep mixity are also figured out.

4.2.1. Normalized stress function

A finite element formula to present the normalized stress function of different stress components is presented as follows. With the presented Eq. (2), the equivalent stress should be written as follows.

$$\sigma_e = \sigma_0 \left(\frac{C^*}{\dot{\varepsilon}_0 \sigma_0 I_n r} \right)^{1/(n+1)} \tilde{\sigma}_e(\theta, n, M^c) \tag{13}$$

where

$$\tilde{\sigma}_e = \sqrt{\frac{3}{2} \tilde{S}_{ij} \tilde{S}_{ij}} \tag{14}$$

Similarly derived as Shlyannikov et al. [33], a numerical method to determine the $\tilde{\sigma}_e$ is presented as below.

$$\tilde{\sigma}_e^{FE} = \sigma_e^{FE} / (\sigma_0 K^{cr}) r^{1/(n+1)} \tag{15}$$

$$\tilde{\sigma}_{ij}^{FE} = \sigma_{ij}^{FE} / (\sigma_0 K^{cr}) r^{1/(n+1)} \tag{16}$$

where the K^{cr} is the creep intensity factor defined in Eq. (8), and i, j are r and θ under two-dimensional condition, respectively. The maximum value of $\tilde{\sigma}_e^{FE}$ is 1. With the presented numerical method, the angular distribution functions can be determined directly. The creep mixity factor can be calculated directly through FE extraction [9].

$$M^c = \frac{2}{\pi} \arctan \left| \frac{\tilde{\sigma}_{\theta\theta}^{FE}(\theta = 0)}{\tilde{\sigma}_{r\theta}^{FE}(\theta = 0)} \right| \tag{17}$$

To verify the variation of the normalized angular stress distribution, the angular distributions of equivalent Mises stress, normal stress, opening stress and shearing stress for shallow and deep cracked CTS specimen are presented in Figs. 10 and 11, respectively.

In these figures, angular stress distributions of two typical loading angles, i.e. 22.5° and 67.5°, under different creep time are selected to present. Clearly, it can be seen that the angular distributions coincide with each other quite well even at creep time of $12t_T$. It can be also found that the maximum location of $\tilde{\sigma}_{\theta\theta}^{FE}$, i.e. the maximum tangential stress (MTS) direction, is almost not changed with the increase of creep time. The reason is that the angular distributions are originally determined by the HRR solutions. If the creep mixity factor is the same, the angular distribution functions are also the same.

With the above verification, the elastic mixity factor and creep mixity factor for the CTS specimen are given in Table 5. It can be seen that the elastic mixity factors agree quite closely with the creep mixity factors for cases with loading angles 0° and 90°. However, there are differences between the values of the elastic mixity factor and creep mixity factor for loading angles 22.5°, 45° and 67.5°.

4.2.2. Angular and radial distribution of opening stress

The angular distributions of opening stress for shallow and deep cracked CTS specimens are presented in Fig. 12 where the solutions are obtained at 1 mm and 2.55 mm away from creep crack tip, respectively. It can be seen that the opening stress of shallow cracked specimen approaches to the mode II case under loading angles 0°, 22.5° and 45°. The maximum opening stress increases slightly with the rise of loading angle, however, the maximum opening stress under mode I case is smaller than that of mode II condition for shallow cracked CTS specimen. It reveals that the mode II type of shallow cracked CTS specimen

Table 3
Fracture parameters for different loading angles of SEN specimen with $a/W = 0.1$.

β	K_I (MPa·mm$^{1/2}$)	K_{II} (MPa·mm$^{1/2}$)	K_{eff} (MPa·mm$^{1/2}$)	C^* (MPa·mm/h)	t_{red} (h)	t_T (h)
0	1.425	105.9	105.91	2.7162E−4	300.636	75.159
22.5	66.64	97.36	117.98	2.1304E−4	475.64	118.91
45	124.5	74.03	144.85	1.001E−4	1525.82	381.455
67.5	163.4	39.49	168.10	2.8613E−05	7189.56	1797.39
90	177.1	1.001	177.1	1.6683E−05	13686.4	3421.6

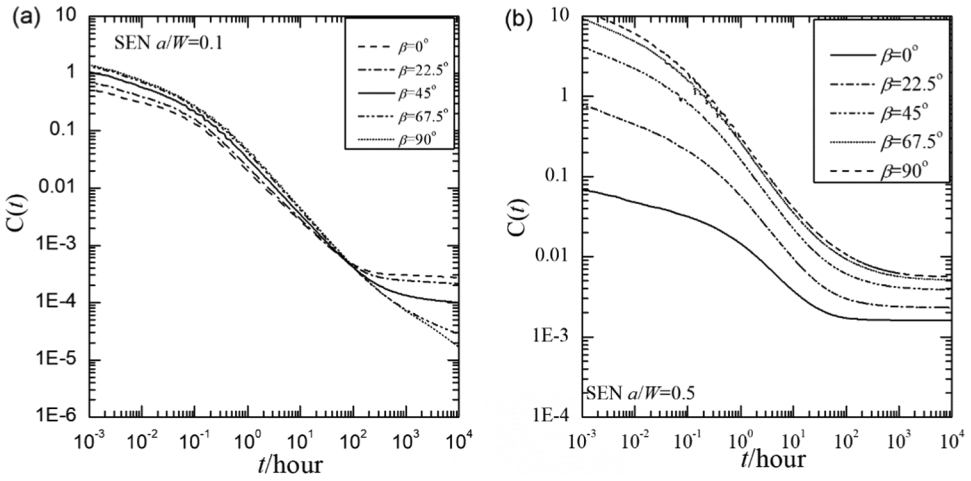

Fig. 5. Variations of $C(t)$ with creep time under different loading angles for SEN specimen with (a) $a/W = 0.1$ and (b) $a/W = 0.5$.

prevails than the mode I case. For deep cracked CTS specimen, the tendencies presented here are quite different in which the maximum value of opening stress for deep cracked CTS specimen increases with the rise of loading angle.

The analytical HRR solutions are also plotted in those figures so as to make a comparison with the numerical solutions, where the solutions have been tabled by Symington et al. [39] and also revisited with asymptotic method for creep crack by Dai et al. [9]. The C^*-integral for the analyzed cases have been listed in Tables 1–4. For shallow cracked CTS specimen, the difference between the HRR field (solid lines in figures) and the FE results (symbols in figures) are not significant though there exists slight differences in some regions. Similar tendencies can be found in the deep cracked CTS specimen (see Fig. 12(b)). Generally speaking, although the discrepancy of angular opening stress for CTS specimen between the HRR field and FE solutions is not remarkable, the difference around the maximum opening stress position of the opening stress is larger than the other locations.

Maximum tangential stress (MTS) direction is considered as the crack initiation criterion. Shlyannikov and Tumanov [40] presented a MTS direction determination method which has been introduced in the Part I of the paper, and it can be written as.

$$\frac{\partial \widetilde{\sigma}_{\theta\theta}}{\partial \theta} = 0, \quad \frac{\partial^2 \widetilde{\sigma}_{\theta\theta}}{\partial \theta^2} < 0 \tag{18}$$

With this definition, the directions of the maximum circumferential stress or maximum tangential stress (MTS) for shallow cracked CTS specimen under loading angles 0°, 22.5°, 45°, 67.5° and 90° are obtained as −67.5°, −63°, −58.5°, −36° and 0°, respectively. The MTS directions for deep cracked CTS specimen under loading angles 0°, 22.5°, 45°, 67.5° and 90° are −58.5°, −45°, −31.5°, −9° and 0°, respectively. It should be mentioned that the opening stresses are obtained at the creep time of 10,000 h which are considered to be under extensive creep as the $C(t)$-integrals show the path-independency.

The radial distributions of the opening stress for shallow and deep cracked along the crack line at 10,000 h are presented in Fig. 13. Theoretically, the opening stress along the crack line for the loading angle 0° is zero due to the anti-symmetry condition under pure mode II case. However, it can be found that the opening stresses for the CTS specimen with $\beta = 0°$ are less than zero with numerical analyses which implies that the crack tip become more severely deformed. This sharpening phenomenon has been found in the experimental observation given by Poquillon et al. [27]. It should be mentioned that the differences between the analytical HRR solutions and the FE results are not significant except for the narrow region near the crack tip. It may reveal that the opening stress along the crack line is not suitable to be used to characterize the constraint effect for the mixed I/II creep crack.

Inspired by the previous MTS criterion, the opening stresses at the transition time t_T along the MTS direction are presented in Fig. 14. It is interesting to find that the deviations between the HRR solutions and the FE results under loading angle 0° are quite small. Similar variations can be found for loading angles 22.5°, 45° and 67.5°. The deviation enlarges for condition with loading angle 90° which is very close to the

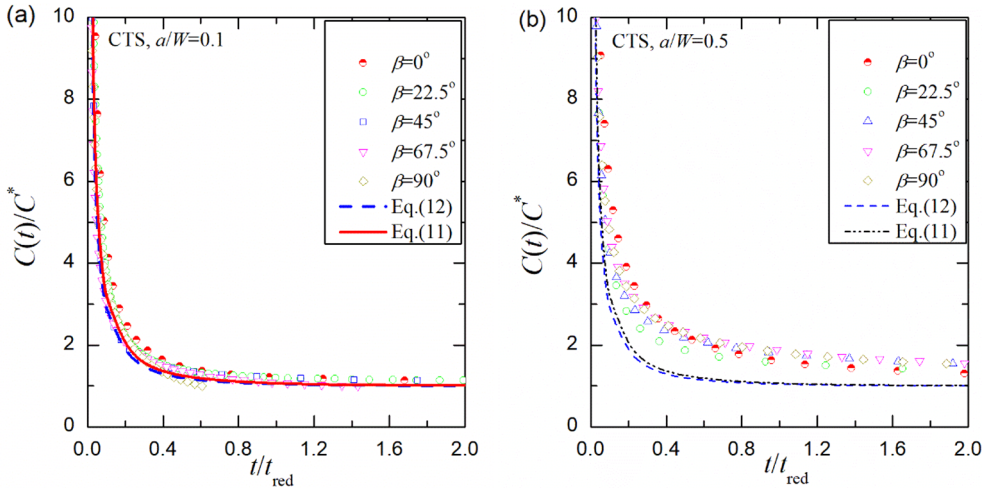

Fig. 6. Variations of $C(t)/C^*$ with normalized creep time under different loading angles for CTS specimens.

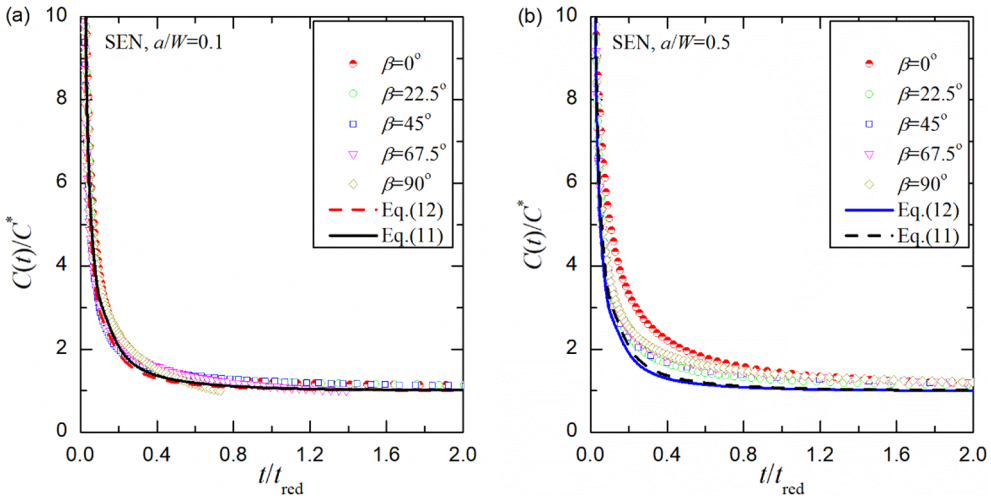

Fig. 7. Variations of $C(t)/C^*$ with normalized creep time under different loading angles for SEN specimens.

mode I case, and it reveals that the loss dominance of $C(t)$ in the MTS direction happens remarkably for the shallow cracked CTS specimen under the case with loading angle 90° which is very close to the pure mode I case. It should be mentioned that the singularity for the stress field of the shallow cracked CTS specimen is kept well, and no obvious blunting effect or sharpening effect occur at the transition time. For the deep cracked CTS specimen (see Fig. 14(b)), the remarkable difference for opening stress along MTS direction between the HRR field and FE solution happens at the case with loading angle 0° (very close to pure mode II case), and the deviation enlarges as if $r > 0.1$ mm. The loss dominance of C^* decreases with the increase of loading angle along the MTS direction for deep cracked CTS specimen. It can be seen that the FE solution coincides with the HRR field quite reasonably for loading angle 90°, i.e. close to pure mode I case.

Fig. 15 is presented to investigate the variations of the opening stress along MTS direction at 10,000 h, which is under extensive creep. For shallow cracked CTS specimen, there exists the blunting influenced region along the crack tip and the differences between the HRR fields and the FE results in the influenced region are quite large. It can be found that the condition with loading angle 0° contains the largest influenced region, while the loading angle 90° contains uninfluenced region. For conditions with loading angles 0°, 22.5°, 45° and 67.5°, the loss dominance of C^* is not remarkable. The condition with loading angle 90° for shallow cracked specimen presents the remarkable loss dominance of C^*.

For deep cracked CTS specimen (see Fig. 15(b)), there are also the finite deformation influenced region for loading angles 0°, 22.5° and 45°, and the blunting influenced region decreases with the increase of the loading angle. The deviations between the HRR solutions and the FE results are not significant for deep cracked CTS specimens except for the blunting affected region. This is different comparing with the tendencies presented at the transition time.

4.2.3. Angular and radial distribution of stress triaxiality

Stress triaxiality, which is defined as the ratio between the hydrostatic stress σ_m and Mises equivalent stress σ_e, is considered as the constraint characterization parameter for the mode I creep crack which is considered to be an important role in the characterizations of fracture process zone [1,39,40].

Herein, the angular distributions of stress triaxiality for shallow and deep cracked CTS specimen are presented in Fig. 16. The stress triaxiality is obtained at 10,000 creep hours at 0.5513 mm and 1.0 mm away from crack tip. It can be seen that there exists the negative region for the specimens if it is under mode II deformation. With the increase of the loading angle, the region of negative stress triaxiality region becomes smaller and smaller. Finally, the negative region disappears if the loading angle approaches to 90°, i.e. very close to mode I case. Clearly, the maximum value of stress triaxiality locates at $\theta = 0°$, while the

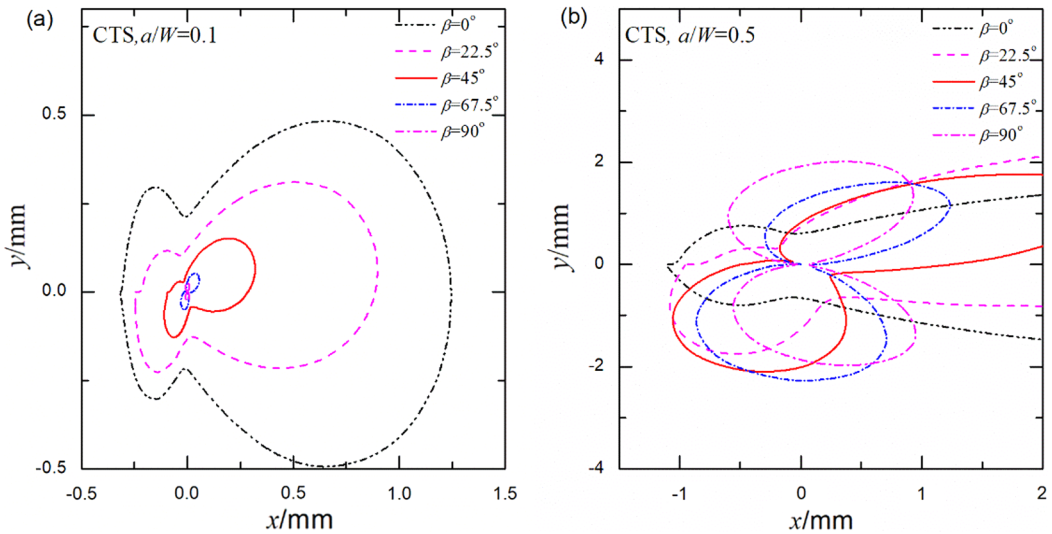

Fig. 8. Equivalent creep strain under different loading angles for CTS specimen of (a) $a/W = 0.1$ and (b) $a/W = 0.5$ at creep time of 10,000 h.

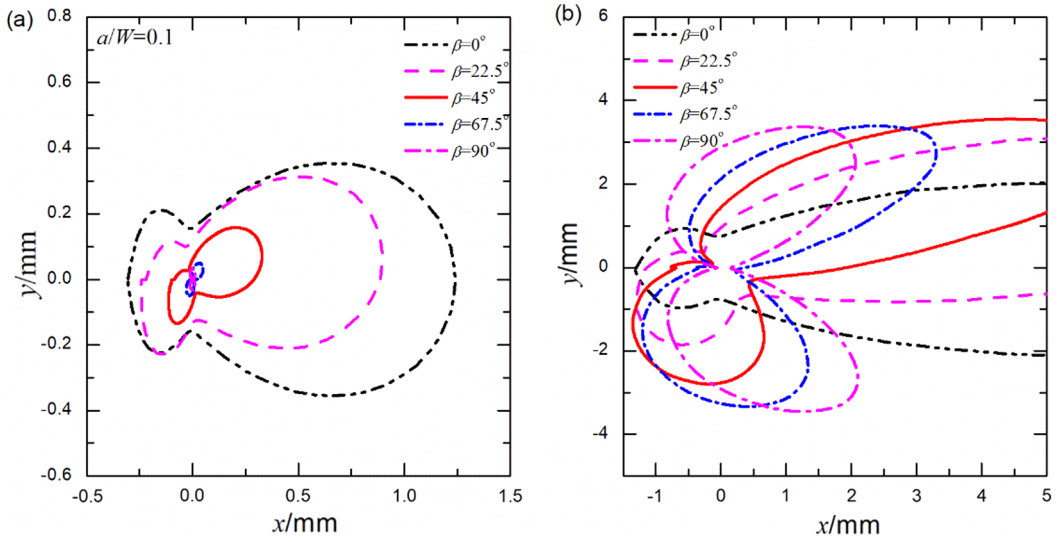

Fig. 9. Equivalent creep zone under different loading angles for SEN specimen with (a) $a/W = 0.1$ and (b) $a/W = 0.5$ at creep time of 10,000 h.

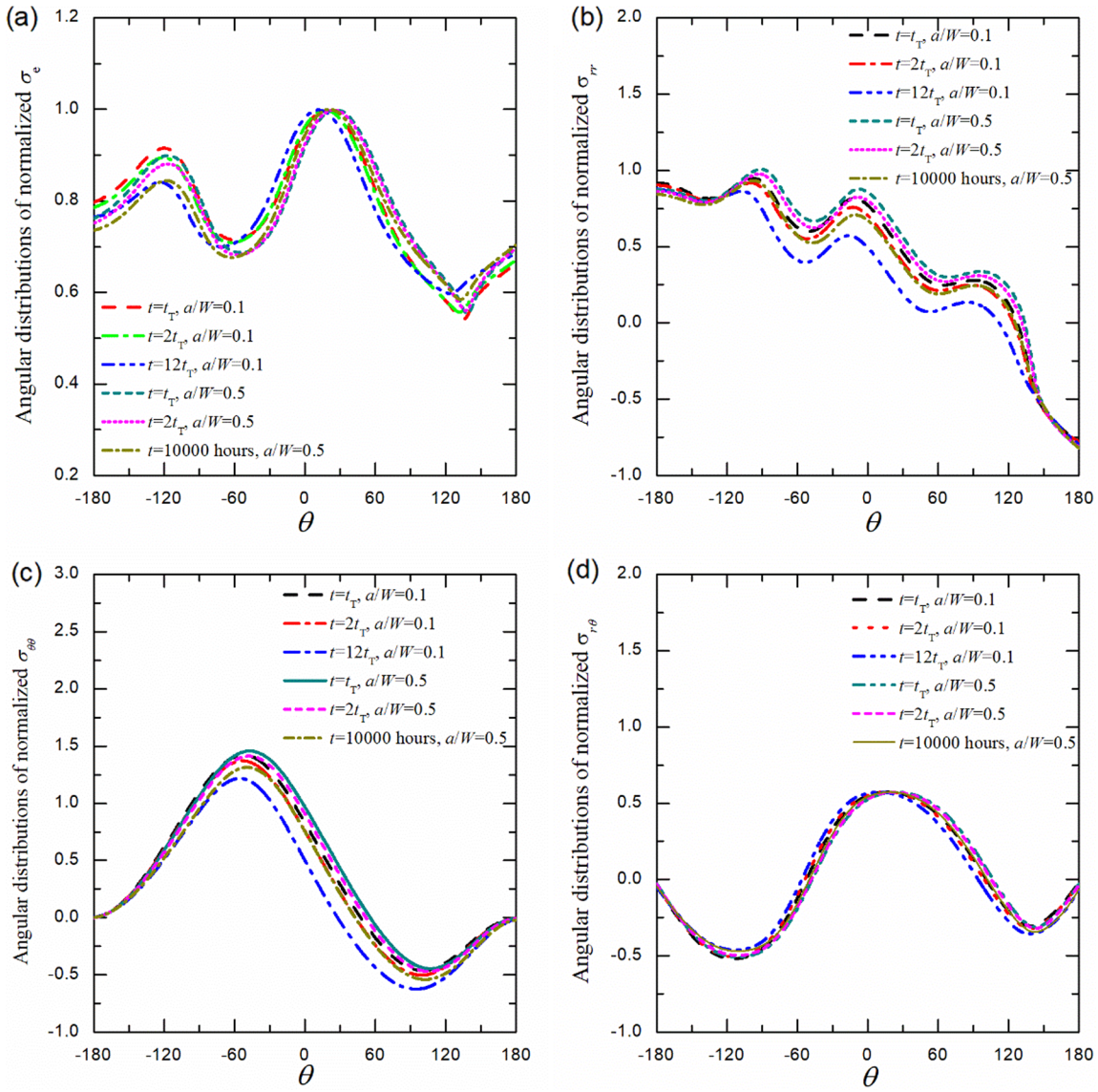

Fig. 10. Angular distributions for normalized stress function of (a) equivalent stress, (b) normal stress, (c) opening stress and (d) shearing stress under loading angle of 22.5°.

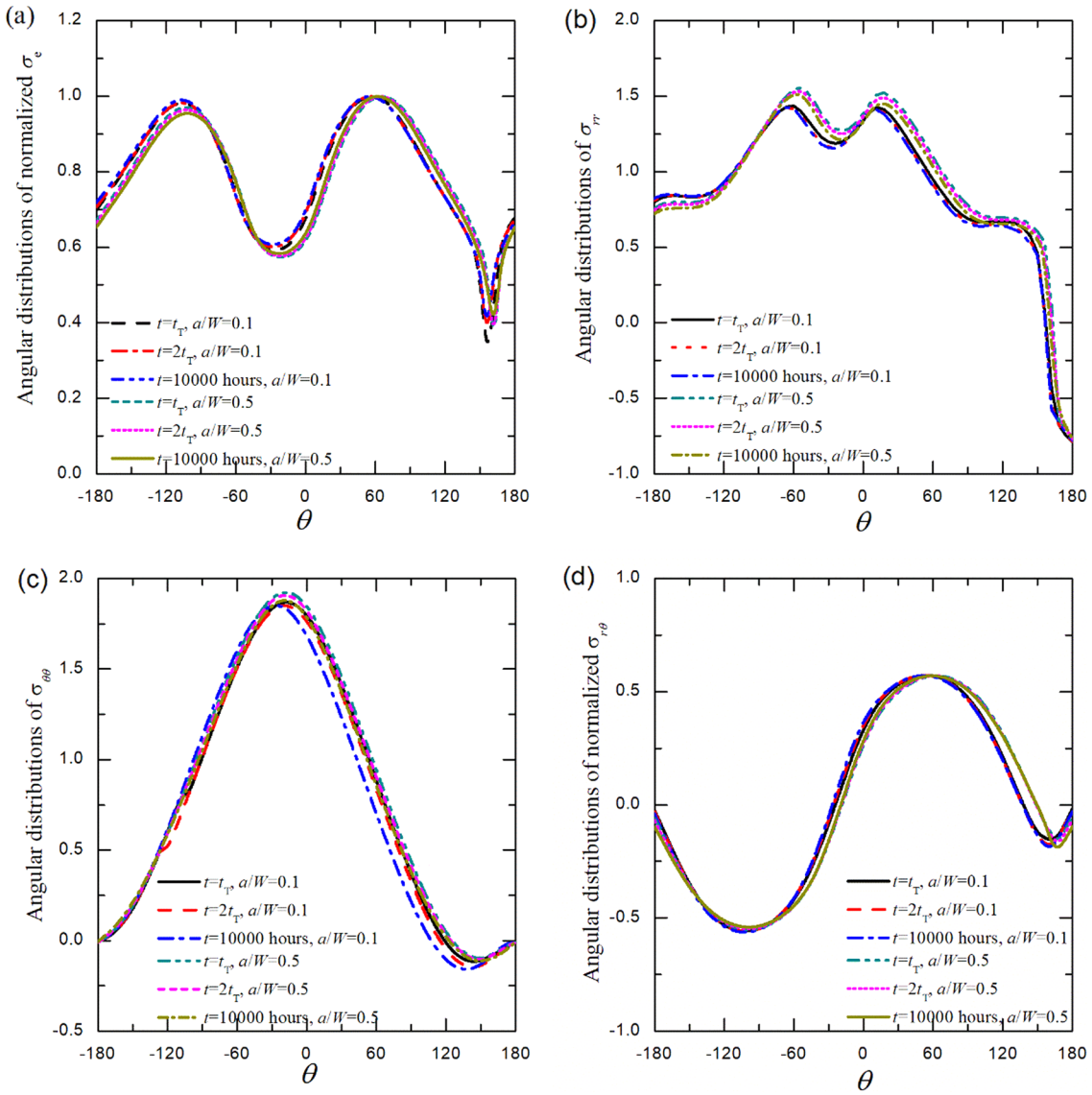

Fig. 11. Angular distributions for normalized stress function of (a) equivalent stress, (b) normal stress, (c) opening stress and (d) shearing stress under loading angle of 67.5°.

Table 5
Mixity factors for CTS specimens.

CTS	Mixity factor	0°	22.5°	45°	67.5°	90°
a/W = 0.1	M^e	0.02864	0.7600	0.8938	0.9537	0.9970
	M^c	0.06404	0.05042	0.4311	0.7939	0.9971
a/W = 0.5	M^e	0.04102	0.3726	0.6452	0.8409	0.9975
	M^c	0.005826	0.5774	0.7889	0.9474	0.9926

location of the maximum stress triaxiality is close to θ = -90° for loading angle 0°. In general, the amplitude of the stress triaxiality under pure mode I case obtains the largest value and smallest value for the mode II case.

To examine the stress triaxiality in the radial direction, the distributions of stress triaxiality for shallow and deep cracked CTS specimens at transition time t_T are shown in Fig. 18. The radial distributions of stress triaxiality are calculated along the MTS direction which have been stated in Section 4.2.2. For shallow cracked CTS specimen, it can be seen that the stress triaxiality is almost independent on the radial distance except for the condition that with loading angle 90° which decreases slightly with the increase of radial distance. For deep cracked CTS specimen, the stress triaxiality is also slightly independent on the radial distance for conditions with loading angles 0°, 22.5° and 45°. The values for stress triaxiality under loading angles 67.5° and 90° decrease with the increase of the radial distance. It implies that the stress triaxiality can be treated as a parameter which is independent on radial distance. For the mixed I/II creep crack, the stress triaxiality along MTS direction can be treated as the radial distance independency.

Fig. 17 is presented to study the influence of creep extent on the radial distributions of stress triaxiality, in which the creep time is 10,000 h. It can be found that the values of stress triaxiality for conditions with loading angles 0°, 22.5°, 45° and 67.5° are independent on the radial distance, however, the stress triaxiality is slightly dependent on the radial distance for condition with loading angle 90°, i.e. mode I case, under extensive creep.

4.3. SEN specimen

4.3.1. Angular distribution of opening stress

As for the SEN specimen, the angular distributions of tangential stress for shallow and deep cracked CTS specimens are presented in Fig. 19 at 10,000 h at fixed distance 1 mm away from crack tip. From

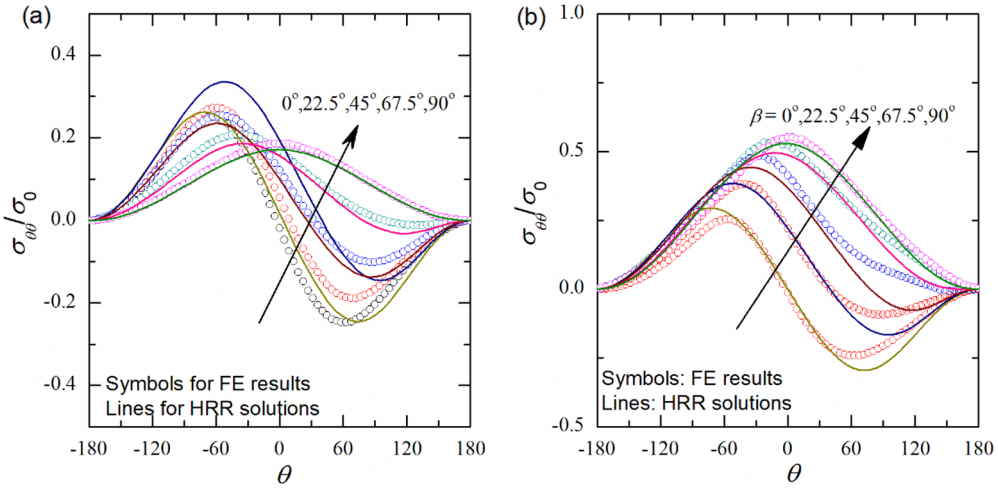

Fig. 12. Comparisons of opening stress in angular direction between HRR field and FE solutions for (a) shallow cracked and (b) deep cracked CTS specimen.

the comparisons between the HRR solutions and FE results, the differences between them are not remarkable. It indicates that the dominance of $C(t)$ in the angular direction seems to be not remarkable. With the MTS criterion, the MTS directions for shallow cracked SEN specimen under conditions with loading angles 0°, 22.5°, 45°, 67.5° and 90° are −67.5°, −63°, −54°, −49.5° and 0°, respectively. For shallow cracked SEN specimens, the amplitude of the opening stress slightly decreases with the increase of loading angle. The MTS directions for deep cracked SEN specimens are −58.5°, −40.5°, −27°, −13.5° and 0°, respectively. For the deep cracked SEN specimen, the opening stress also increases with the rise of loading angle.

The elastic mixity and creep mixity factor are presented in Table 6. It can be seen that there is the difference between the elastic mixity factor and creep mixity factor. It can be found that the elastic mixity factors are always higher than the creep mixity factors under the cases with loading angles 22.5°, 45° and 67.5°. For cases with loading angles 0° and 90°, the creep mixity factors are almost close to the elastic mixity factors.

4.3.2. Radial distribution of opening stress

The opening stresses along the crack line at 10,000 h for the shallow and deep cracked SEN specimens are presented in Fig. 20. It can be seen that the opening stresses for the SEN specimens under loading angles 0° and 22.5° deviate from the HRR solutions quite significantly in a small region. The deviation occurs at loading angles 0°, 22.5° and 45° due to the influence of crack tip deformation for both shallow and deep cracked SEN specimens. The analytical HRR fields under loading angles 67.5° and 90° coincide with the FE solutions quite well. It indicates that there are almost no loss dominance of C^* along the crack line for loading angles 67.5° and 90°. This phenomenon is quite different from the conclusions of elastoplastic material which means that the tangential stress along the crack line is not suitable to quantify the loss dominance of $C(t)$-integral for mixed mode I/II creep crack.

Thereafter, the radial distributions of opening stresses along the MTS directions under different loading angles are presented in Fig. 21. It can be seen that the deviations between the HRR field and the FE solutions are quite large for shallow cracked SEN specimens. It reveals that the loss dominance of $C(t)$ for the shallow cracked SEN specimen is remarkable than that of the shallow cracked CTS specimen. For the deep cracked CTS specimen, it can be found that the deviations between HRR solutions and FE results for loading angles 0° and 22.5° are significant as if $r > 0.1$ mm, and the situation is very alike the deep CTS specimen.

Furthermore, the opening stresses for the SEN specimens along the MTS direction at the creep time of 10,000 h, i.e. the extensive creep, are given in Fig. 22. It can be seen that the opening stresses presented here are quite different with the tendencies shown in Fig. 20. From Fig. 22, the cases with loading angle 0° show the largest blunting region for both shallow and deep cracked SEN specimens, while the loading angles 22.5° and 45° present the smaller blunting region. Except for the

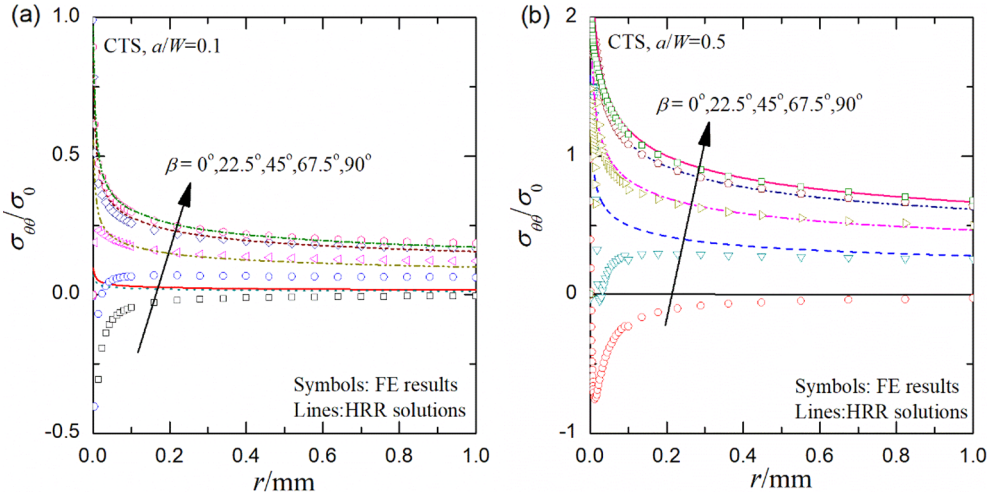

Fig. 13. Comparisons of opening stress in radial distribution between the HRR field and FE solutions for (a) shallow and (b) deep cracked CTS specimen.

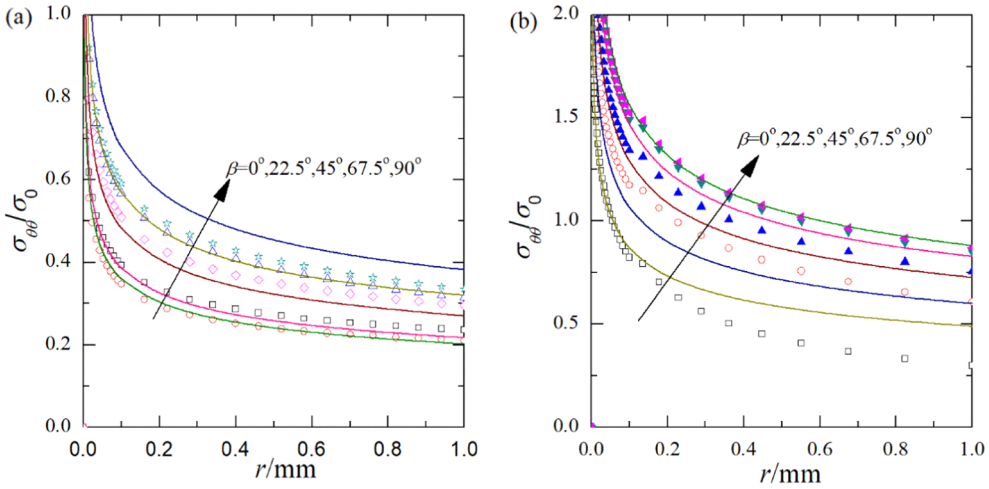

Fig. 14. Comparison of the opening stress along the MTS direction for CTS specimen of (a) $a/W = 0.1$ and (b) $a/W = 0.5$.

blunting affected region, the differences between the HRR solutions and FE results are not significant.

4.3.3. Angular and radial distribution of stress triaxiality

Similar to the CTS specimen, the angular distributions of stress triaxiality under various loading angles for shallow and deep cracked SEN specimens are presented in Fig. 23. It can be found that the stress triaxiality for the SEN specimen increases with the rise of the loading angle. The stress triaxiality for the loading angle 0°, i.e. pure mode II case, is anti-symmetric along the crack line. However, the stress triaxiality under loading angle 90° (mode I case) is symmetric along the crack line, and there is no negative region for the mode I case. The amplitude of the stress triaxiality presents the higher value for the deep cracked SEN specimen than shallow cracked SEN specimen.

Similarly, the radial distributions of stress triaxiality along the MTS direction are presented in Fig. 24. It can be seen that values of stress triaxiality in radial direction for cases with loading angles 0°, 22.5°, 45° and 67° are independent on the radial distance for the shallow cracked SEN specimen. However, the stress triaxiality for the loading angle 90° decreases with the increase of the radial distance. It should be mentioned that the values of stress triaxiality for both shallow and deep cracked SEN specimen are obtained at 10,000 h. For the deep cracked SEN specimen, the values of stress triaxiality for loading angles 0°, 22.5°, 45° and 67.5° are almost not dependent on the radial distance away from crack tip. The stress triaxiality increases with the rise of the loading angle, which implies that the mode I creep crack presents the highest stress triaxiality than those of the other conditions.

To show the variations stress triaxiality of the mixed I/II creep crack with creep time, the stress triaxiality at one times of transition time and two times of transition time for the shallow cracked specimens are presented in Fig. 25. It can be found that the values of stress triaxiality for loading angles 0°, 22.5°, 45° and 67.5° are almost independent on the distance no matter whether the creep time is one time of transition time or two times of transition time. Compared with the stress triaxiality under the longer transition time, the variations of stress triaxiality are slight.

The variations of the stress triaxiality for the deep cracked SEN specimen are presented in Fig. 25. It can be seen that the stress triaxiality is also slightly dependent on the distance away from the crack tip. With the increase of the creep time, the slope along the radial distance for the stress triaxiality becomes smaller. However, the stress triaxiality is slightly independent on the radial distance for condition with loading angles 67.5° and 90°.

Comprehensively considering the results mentioned above, the stress triaxiality for the SEN specimen for the mixed I/II creep crack is independent on the radial distance if it is under extensive creep. However, the stress triaxiality under the condition close to the mode I case seems to be not independent on the radial distance. The results also indicate that the stress triaxiality along the MTS direction for the mixed mode type creep crack can be used as a constraint parameter.

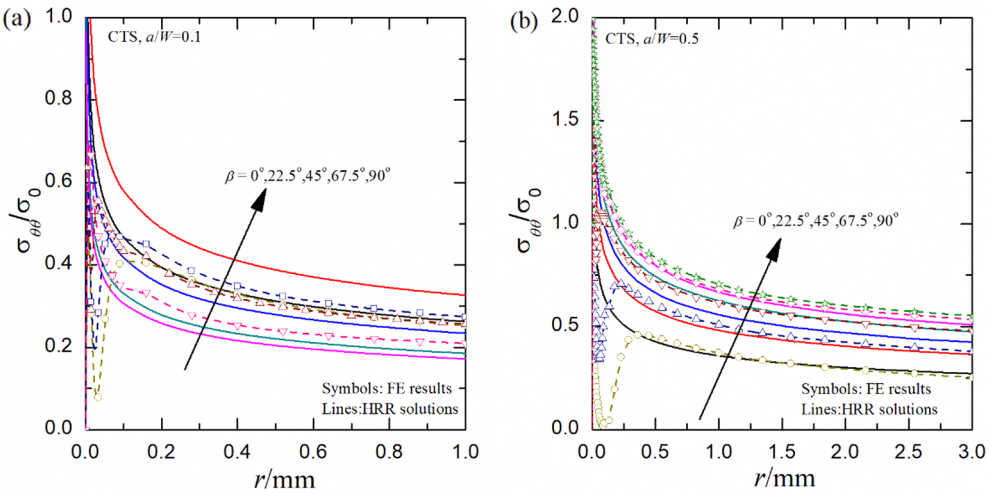

Fig. 15. Comparison of the opening stress along the MTS direction for CTS specimen at of (a) $a/W = 0.1$ and (b) $a/W = 0.5$ at creep time of 10,000 h.

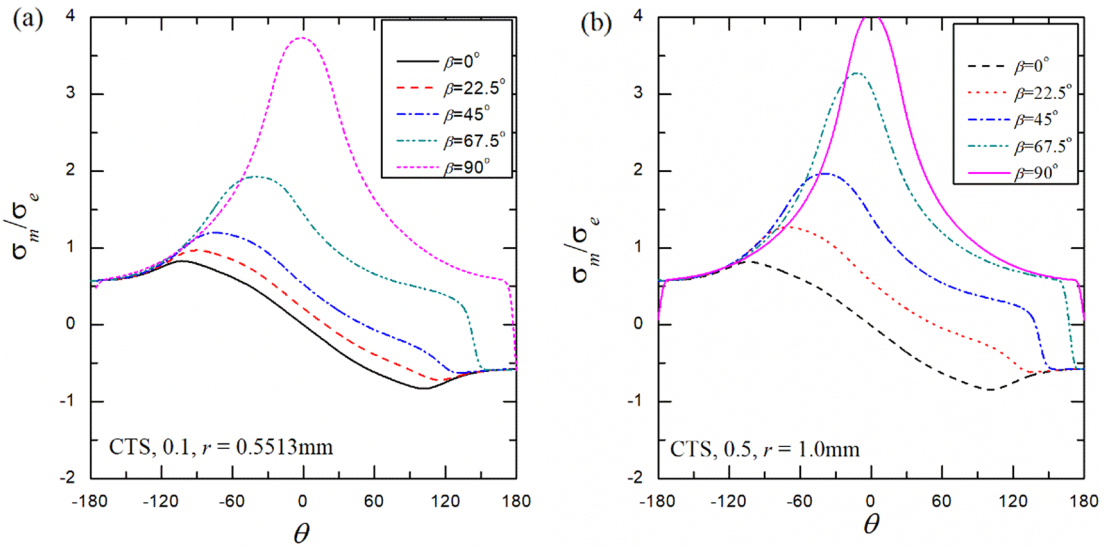

Fig. 16. Angular distributions of stress triaxiality under different loading angles for (a) shallow and (b) deep crack CTS specimen.

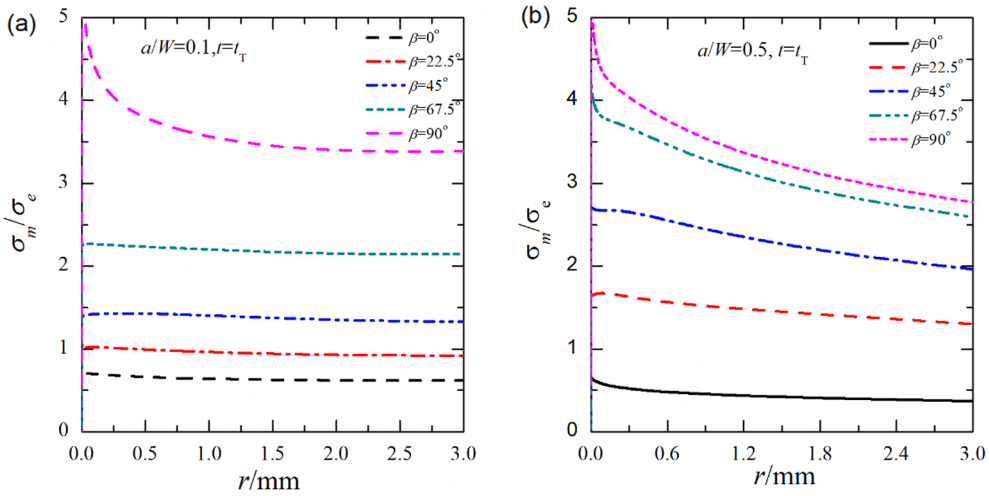

Fig. 17. Radial distributions of stress triaxiality in MTS direction for (a) shallow and (b) deep cracked CTS specimen.

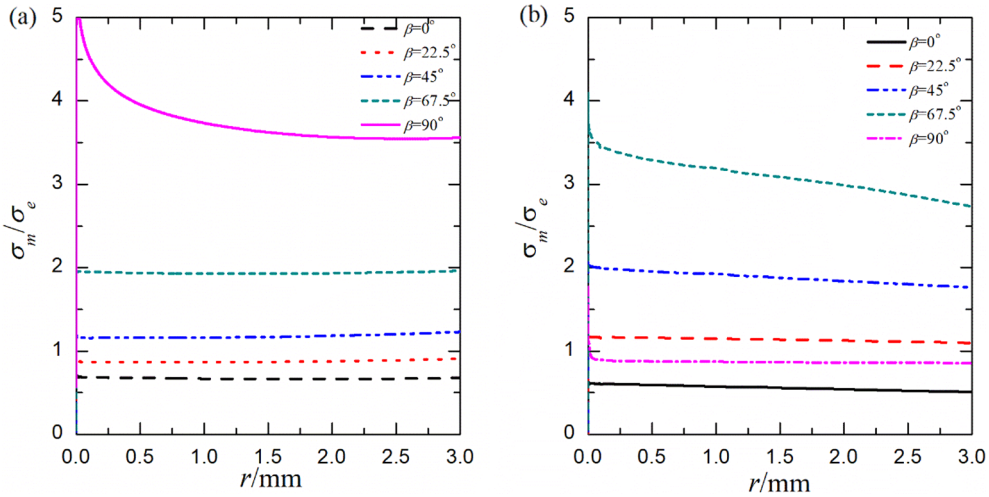

Fig. 18. Radial distributions of stress triaxiality in MTS direction for (a) shallow and (b) deep cracked CTS specimen at 10,000 h.

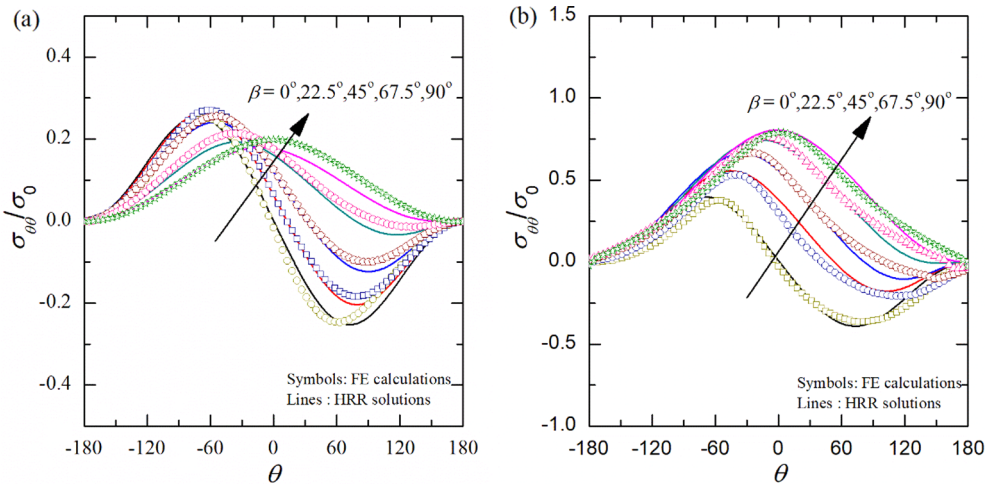

Fig. 19. Distributions of opening stress at fixed distance of $r = 1$ mm for (a) shallow and (b) deep cracked SEN specimen.

Table 6
Elastic and creep mixity factors for SEN specimens.

SEN	Mixity factor	0	22.5	45	67.5	90
$a/W = 0.5$	M^e	0.02506	0.7482	0.8882	0.9513	0.9969
	M^c	0.00601	0.6739	0.8024	0.9288	0.9953
$a/W = 0.1$	M^e	0.008566	0.3821	0.6585	0.8490	0.9964
	M^c	0.008313	0.2418	0.5045	0.7905	0.9443

4.4. Discussions

4.4.1. Applicability of Q-parameter

Generally, the constraint parameter for the mode I case is presented as [41,42]

$$Q = \frac{\sigma_{\theta\theta} - \sigma_{\theta\theta}^{\mathrm{HRR}}}{\sigma_0} \quad \theta = 0^{\mathrm{o}} \tag{19}$$

in which $\sigma_{\theta\theta}^{\mathrm{HRR}}$ is the opening stress of the HRR field along the crack line. The above form is directly introduced into creeping material for mode I creep crack by Shih et al. [41] and Budden and Ainsworth [42]. For mixed mode I/II creep crack, the Q-parameter is just introduced and presented in Fig. 26 in order to investigate the applicability of Q-parameter. It can be found that the Q-parameter for both shallow and deep cracked SEN specimens is strongly dependent on the radial distance under loading angle 0°, which is close to mode I case.

Based on the above analysis, the Q-parameter defined ahead of the crack line in the fracture process zone is not suitable to be used as the constraint parameter for the mixed I/II creep crack tip field under extensive creep. Herein, we proposed a constraint parameter for the mixed mode extensive creep crack as follows.

$$Q^* = \frac{\sigma_m}{\sigma_e} - \left(\frac{\sigma_m}{\sigma_e}\right)_{REF} \quad \theta = \theta_{\mathrm{MTS}} \tag{20}$$

where $(\sigma_m/\sigma_e)_{REF}$ is the stress triaxiality of the reference stress field, and the selection of the reference stress field can be selected as a mixed mode crack tip with a deep cracked specimen. θ_{MTS} is the direction of MTS. It should be noted that the Q^* can present the difference between the analyzed stress field and the reference stress field directly. The SEN specimens is adopted to present the Q^*-parameter under various conditions (see Fig. 27). It should be pointed out that the Q^*-parameter is obtained at the creep time of 10,000 h.

4.4.2. Influence of loading

Though the influence of geometry size on the mixed I/II creep crack tip has been analyzed, the effect of loading on the creep crack tip field is unclear yet. Herein, Fig. 29 is presented to investigate the influence of loading level on the opening stress along MTS direction for the shallow cracked SEN specimens. Three shallow cracked SEN specimens, i.e. cases with loading angles 22.5°, 45° and 67°, under three different loading levels are adopted, i.e. 0.5 kN, 1 kN and 1.5 kN, respectively.

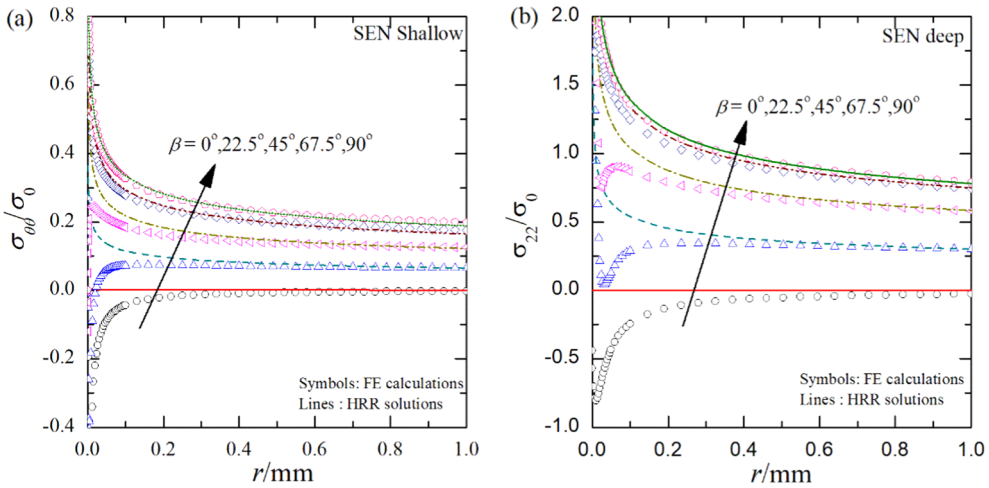

Fig. 20. Comparison of opening stress along crack line between HRR field and FE solutions for (a) shallow and (b) deep cracked SEN specimens.

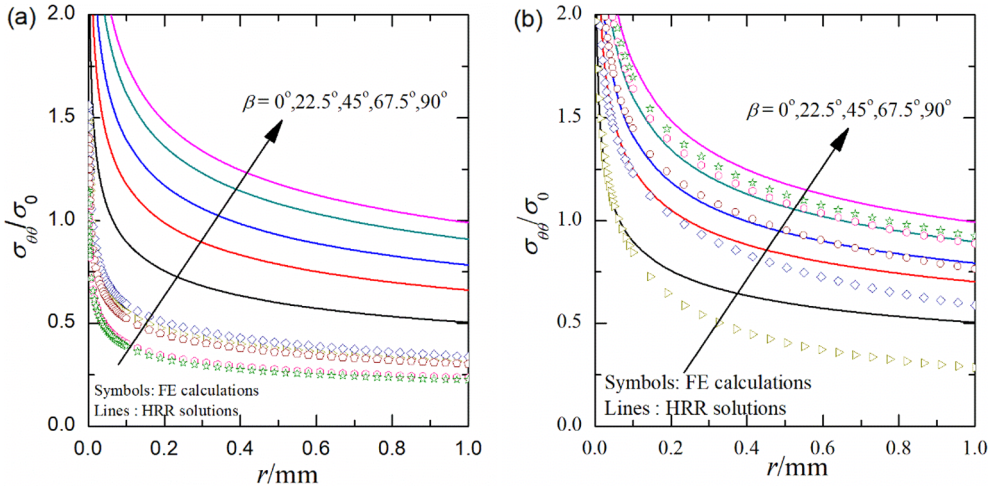

Fig. 21. Variations of dimensionless opening stress along the MTS direction for (a) shallow SEN specimen and (b) deep SEN specimen at the transition time.

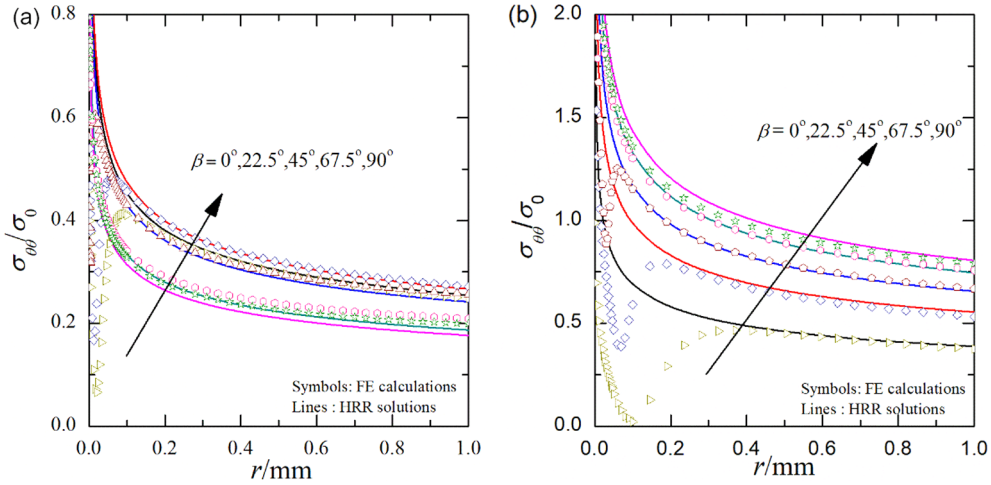

Fig. 22. Variations of dimensionless opening stress along the MTS direction for (a) shallow SEN specimen and (b) deep SEN specimen at 10,000 h.

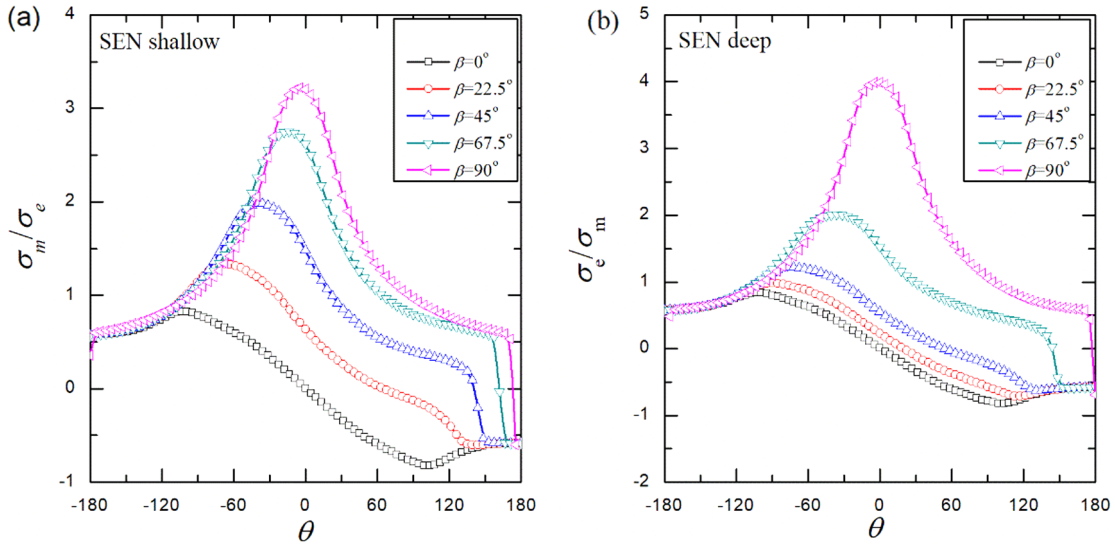

Fig. 23. Variations of stress triaxiality for SEN specimens for (a) $a/W = 0.1$ and (b) $a/W = 0.5$.

For case under loading angle 22.5°, the C^*-integrals under three different loading levels are 1.43E−05 N mm/h, 2.1304E−4 N mm/h and 1.034E−3 N•mm/h, respectively. From Fig. 28(a), it can be seen that the drop of tangential stress near the crack tip enlarges with the increase of loading level. It reveals that the deformation along the MTS direction increases under the case with loading angle 22.5°. However,

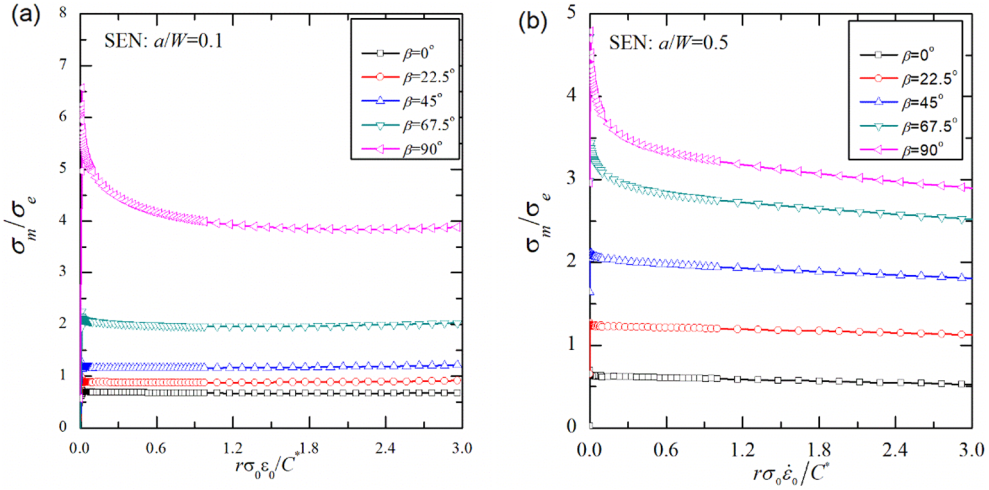

Fig. 24. Variations of stress triaxiality under different loading angles for shallow cracked SEN specimens at (a) t_T and (b) $2t_T$.

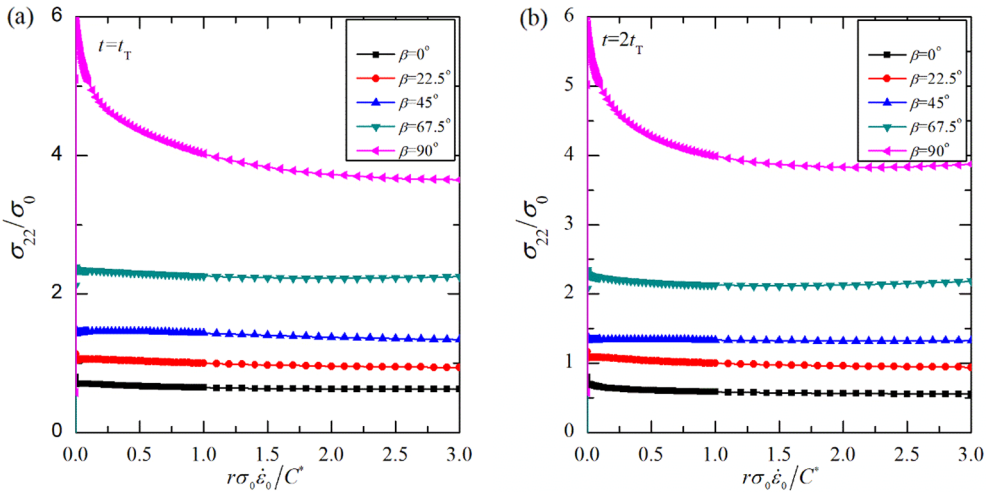

Fig. 25. Variations of stress triaxiality under different loading angles for deep cracked SEN specimens at (a) t_T and (b) $2t_T$.

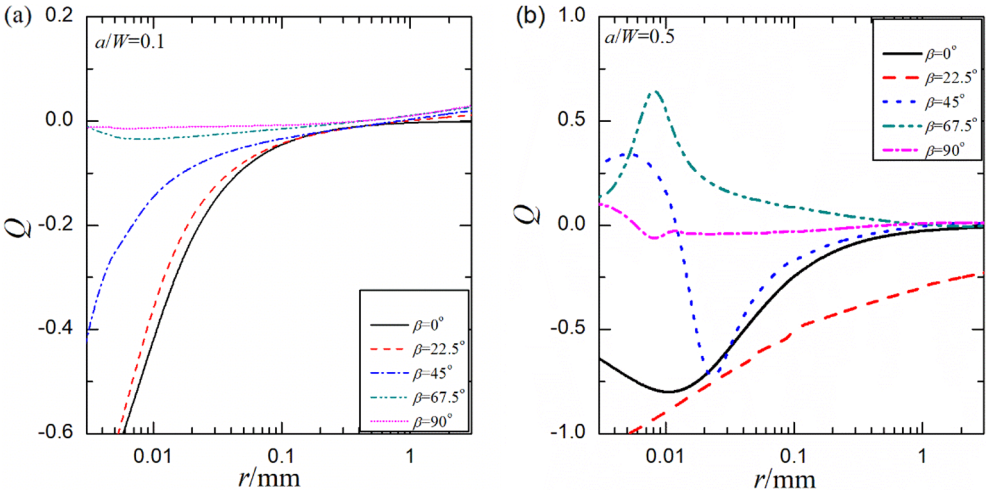

Fig. 26. Variations of Q-parameter along the crack line under different loading angles.

the maximum difference between the HRR field and FE solutions happens under the loading level 0.5 kN. In general, the deviation between the HRR field and FE solution is not remarkable for the case under loading angle 22.5°.

For the case with loading angle 45°, the C^*-integrals for the three loading levels are 7.14E−06 N mm/h, 0.000100107 N mm/h and 0.00048289 N mm/h, respectively. Compared with the condition under loading angle 22.5°, the blunting region is much less under this case. There is a small blunting region under the condition with loading 1.5 kN. For case with loading angle 67.5°, the values of C^*-level are

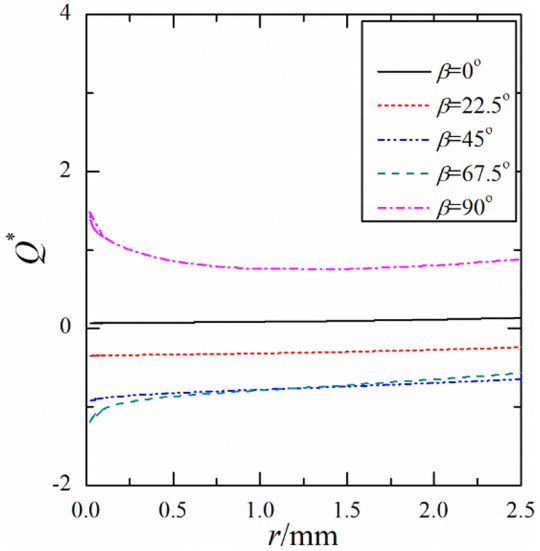

Fig. 27. Variations of Q^*-parameter along the crack line under different loading angles.

3.02056E−06 N mm/h, 2.86129E−05 N mm/h and 0.000119186 N mm/h, respectively. There is no obviously large deformation ahead of creep crack front for the loading angle 67.5° even under 1.5 kN.

For deep cracked SEN specimens, the blunting regions are remarkable for the cases with loading angles 22.5° and 45°. For loading angle 67.5°, the blunting region only occurs at the large loading level, i.e. 1.5 kN. In general, the loss dominance of C^* is also not significant. The stress triaxiality is also presented in Fig. 30. It can be seen that the values of stress triaxiality for SEN specimens are still independent on the radial distance even for the larger loading level. It indicates that the stress triaxiality is independent on the radial distance even for the higher loading level. For loading angles 22.5° and 45°, the values of stress triaxiality are almost not affected by the loading level even the loading approaches to 1.5 kN. It should be pointed out that the stress triaxiality can be influenced by the loading level when the loading level increases.

4.4.3. Influence of blunting effect

To investigate the influence of blunting effect, the stress fields for the mixed mode type creep crack with blunted crack tip are presented in Figs. 31–33. The values of the stress triaxiality in the angular direction at 10,000 creep hours for the blunted crack tip are given in Fig. 31. The results here are calculated under the same loading level as the mode I case. Clearly, it can be seen that the stress triaxiality of the blunted crack shows the same tendency as the sharp one.

The angular distributions of the tangential stress under different loading angles for shallow and deep cracked CTS specimen at creep time 10,000 h are given in Fig. 32. It can be seen that the difference

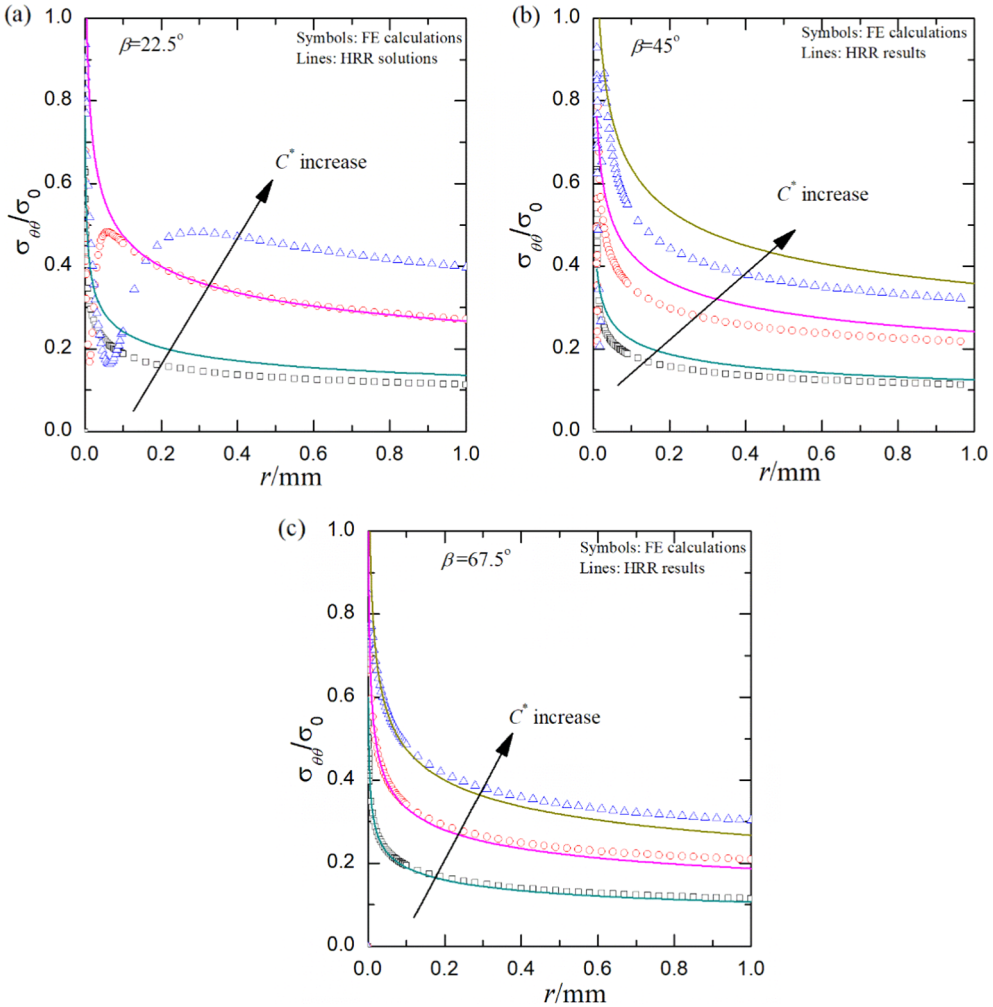

Fig. 28. Variations of opening stress along the MTS direction for SEN specimen with $a/W = 0.1$ under different loadings for (a) $\beta = 22.5^{o}$ (b) $\beta = 45^{o}$ and (c) $\beta = 67.5^{o}$.

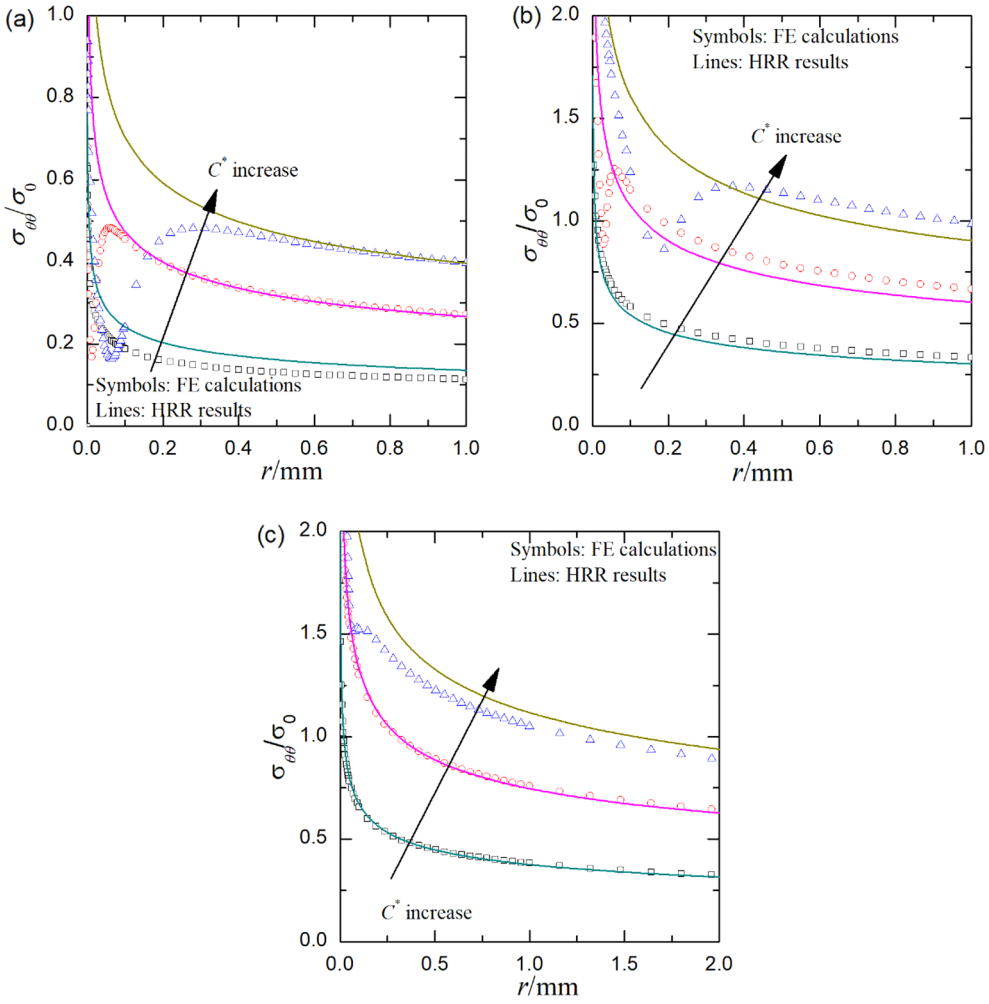

Fig. 29. Variations of opening stress along the MTS direction for SEN specimen with $a/W = 0.5$ under different loadings for (a) $\beta = 22.5^{o}$ (b) $\beta = 45^{o}$ and (c) $\beta = 67.5^{o}$.

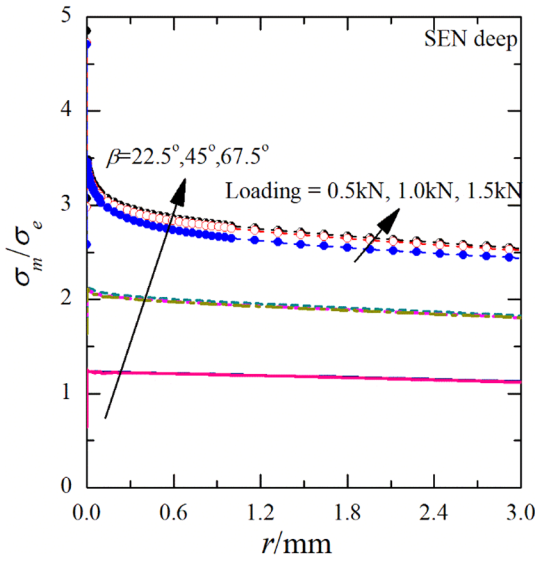

Fig. 30. Variations of stress triaxiality for SEN specimens under different loading levels for $a/W = 0.5$.

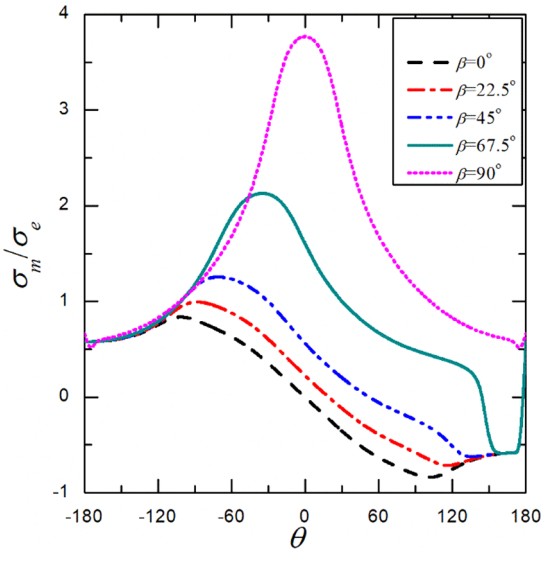

Fig. 31. Variations of stress triaxiality under different loading angles for deep cracked CTS specimen with blunted crack tip.

between the HRR field and FE solution for shallow cracked specimen is not significant. For deep cracked specimens, the deviations between HRR field and FE solutions are remarkable in some regions. The tangential stresses for the shallow and deep cracked specimens are presented in Fig. 33. It can be seen that the differences between HRR field and FE solution are not remarkable for cases with loading angles

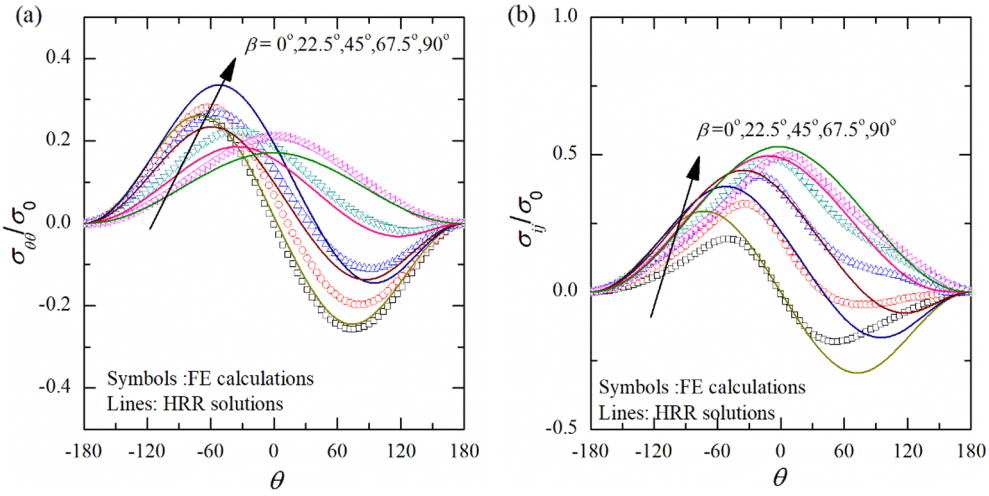

Fig. 32. Comparisons of the opening stress in angular direction between HRR field and FE solutions under different loading angles for blunted CTS specimen of (a) $a/W = 0.1$ and (b) $a/W = 0.5$.

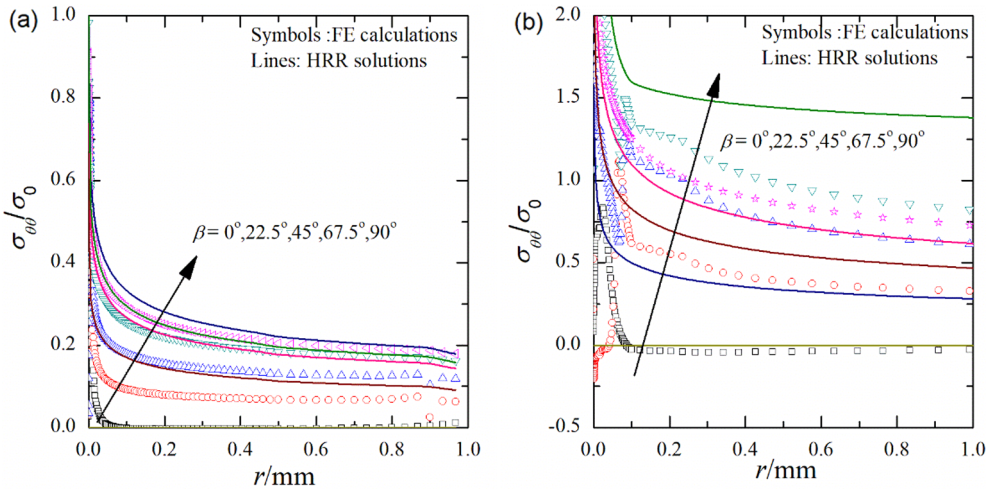

Fig. 33. Comparisons of the opening stress in radial direction between HRR field and FE solutions under different loading angles for blunted CTS specimen of (a) a/$W = 0.1$ and (b) a/$W = 0.5$.

0°, 22.5°, 45°, 67.5°. However, the differences between the HRR fields for loading angle 90° are more remarkable than the other cases. Similar conclusions can be obtained from Fig. 33(b) for deep cracked specimens, i.e. the loss dominance of C^* under loading angle 90° presents to be most remarkable.

Compared with the solutions given in the Part I of this paper, the solutions given in the Part II are more close to the actual conditions for structures serviced at high temperature. For extensive creep, large accumulation of creep strain may occur which could accelerate the damage process where the blunting effect or sharpening effect may become more severe.

5. Concluding remarks

In the part II of this paper, the dominance of the C^*-integral for the mixed I/II crack under extensive creep regime is studied. With various CTS specimens and SEN specimens under different loadings, the stress fields of the mixed I/II creep crack are investigated with different considerations. The conclusions for the mixed I/II creep crack under extensive creep are summarized as follows:

(1) The variations of C^*-integral for the shallow cracked SEN and CTS specimen under mixed loading show that the condition with largest loading angle has the lowest value compared with the other mixed mode conditions. However, the highest the C^*-level appears at the largest loading for the deep cracked specimen. The existed $C(t)/C^*$ and t/t_T relations are presented and discussed for the mixed I/II creep crack which is verified that those relations can be extended to mixed I/II creep crack.

(2) The evolutions of equivalent creep strain for the mixed I/II creep crack tip field are presented. It can be found that the mode II condition contains the largest area for equivalent creep zone among the analysed cases. The equivalent creep zone decreases with the increase of the loading angle (or mixity factor) which implies that the mode I condition possesses the smallest equivalent creep zone under the same loading level. Moreover, it can be seen that the loss dominance of C^* increases with the improvement of loading angle.

(3) Results show that different geometry sizes can lead to different creep mixity factors for the mixed I/II creep crack with CTS and SEN specimens. For the shallow cracked specimens, the specimens for creep mixity factor with loading angle 22.5° are close to the pure mode II. However, the specimens for creep mixity factors with loading angle 22.5° are larger than those cases which are close to the mode I case for the deep cracked specimens.

(4) The loss dominance of C^* is remarkable for those cases which are close to mode I. However, the loss dominance of C^* is not

remarkable for those cases which are close to mode II. The blunting effect heightens with the increase of the loading angle.

(5) A new constraint characterization parameter Q^* for mixed I/II creep crack is proposed which is defined with the difference of stress triaxiality along the MTS direction. The stress triaxiality for the mixed I/II creep crack along MTS direction is independent on the radial distance away from the crack tip under extensive creep. The Q-parameter defined in the mode I case is not suitable to be selected as the constraint effect characterization parameter for mixed I/II creep crack.

The solutions presented in this paper show that the mixed I/II creep crack tip field is more complex compared with pure mode I and pure mode II crack cases. In general, the dominance of $C(t)$ can be characterized along the direction of maximum tangential stress through evaluation of stress triaxiality and equivalent creep zone.

Declaration of Competing Interest

We declare that we have no financial and personal relationships with other people or organizations that can inappropriately influence our work, there is no professional or other personal interest of any nature or kind in any product, service or company that could be construed as influencing the position presented in the paper entitled.

Acknowledgement

The authors acknowledges the supports from the National Natural Science Foundation of China (11902009, 11672009, 11672147, 11872364), the Beijing Natural Science Foundation (2204074), the Scientific Research Common Program of Beijing Municipal Commission of Education (KM202010005034) and CAS Pioneer Hundred Talents Program.

Appendix A

The evolutions of equivalent creep region for mixed creep crack tip of shallow CTS specimen with creep time under various creep mixity factors are shown in Fig. A1. The isoline of equivalent creep strain is identical to 0.05 for those analyzed cases. In general, the equivalent creep zone enlarges with the increase of creep time. The shapes of equivalent creep zone sizes are dependent on the loading angle, i.e. creep mixity factor. It can be found that case under mode I condition possesses smallest creep area. It indicates that the dominance of $C(t)$ or HRR field is most significant under mode II case and less remarkable for mode I case. It implies that the constraint effect for mode I case may be more remarkable under the same loading conditions and should be considered carefully. It should be noted that similar variation tendencies can be found for SEN specimens under mixed mode loadings.

The evolutions of equal equivalent stress with creep time are also presented here which can be found in Fig. A2 where the representative evolution boundaries ($\beta = 0^\circ, \beta = 45^\circ$ and $\beta = 90^\circ$) of equal equivalent stress with creep time are also given. The level of equal equivalent stress here is identical to $0.889\sigma_0$. It can be found that the equal equivalent stress under creep condition is rather different from that of elasoplastic condition due to stress relaxation caused by creep. Under elastoplastic condition, the equal equivalent stress region increases with the improvement of loading

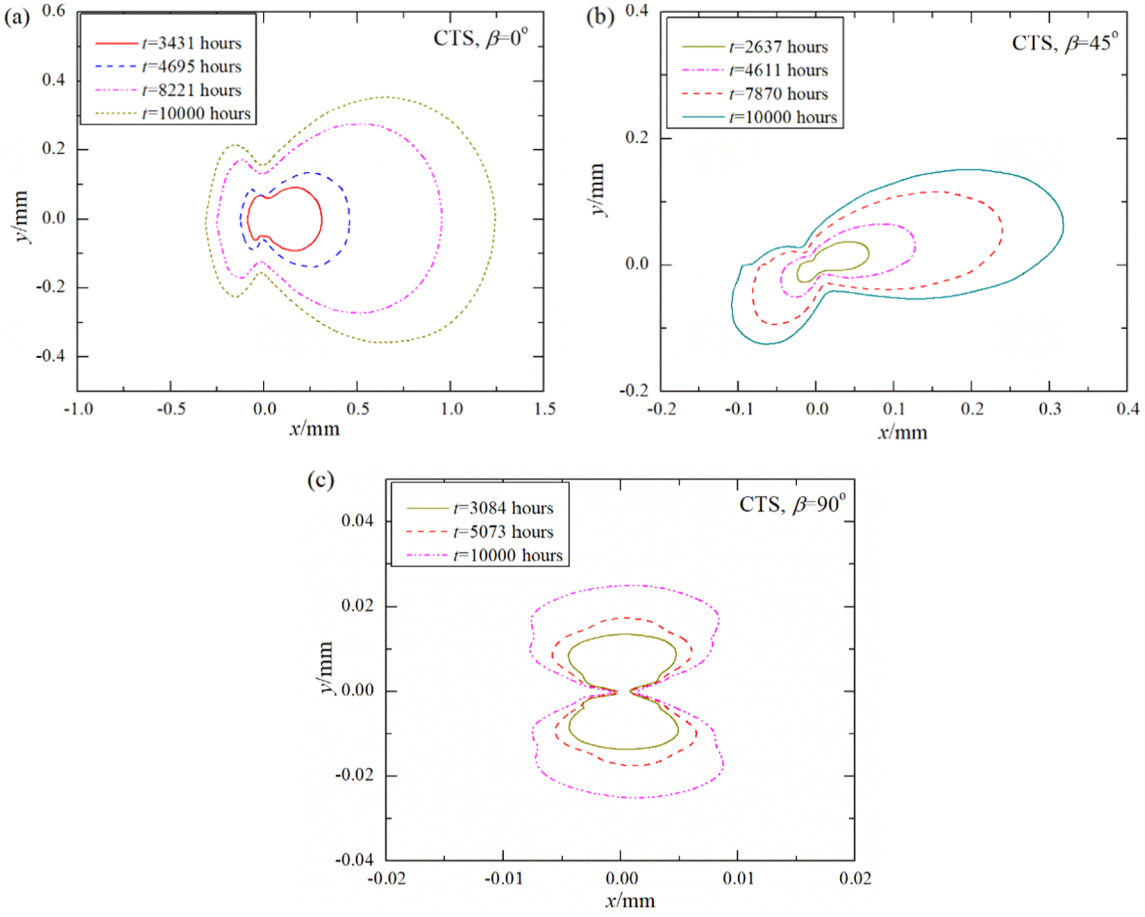

Fig. A1. Evolutions of equivalent creep strain with creep time for different shallow CTS specimens (a) $\beta = 0^\circ$, (b) $\beta = 45^\circ$, (c) $\beta = 90^\circ$.

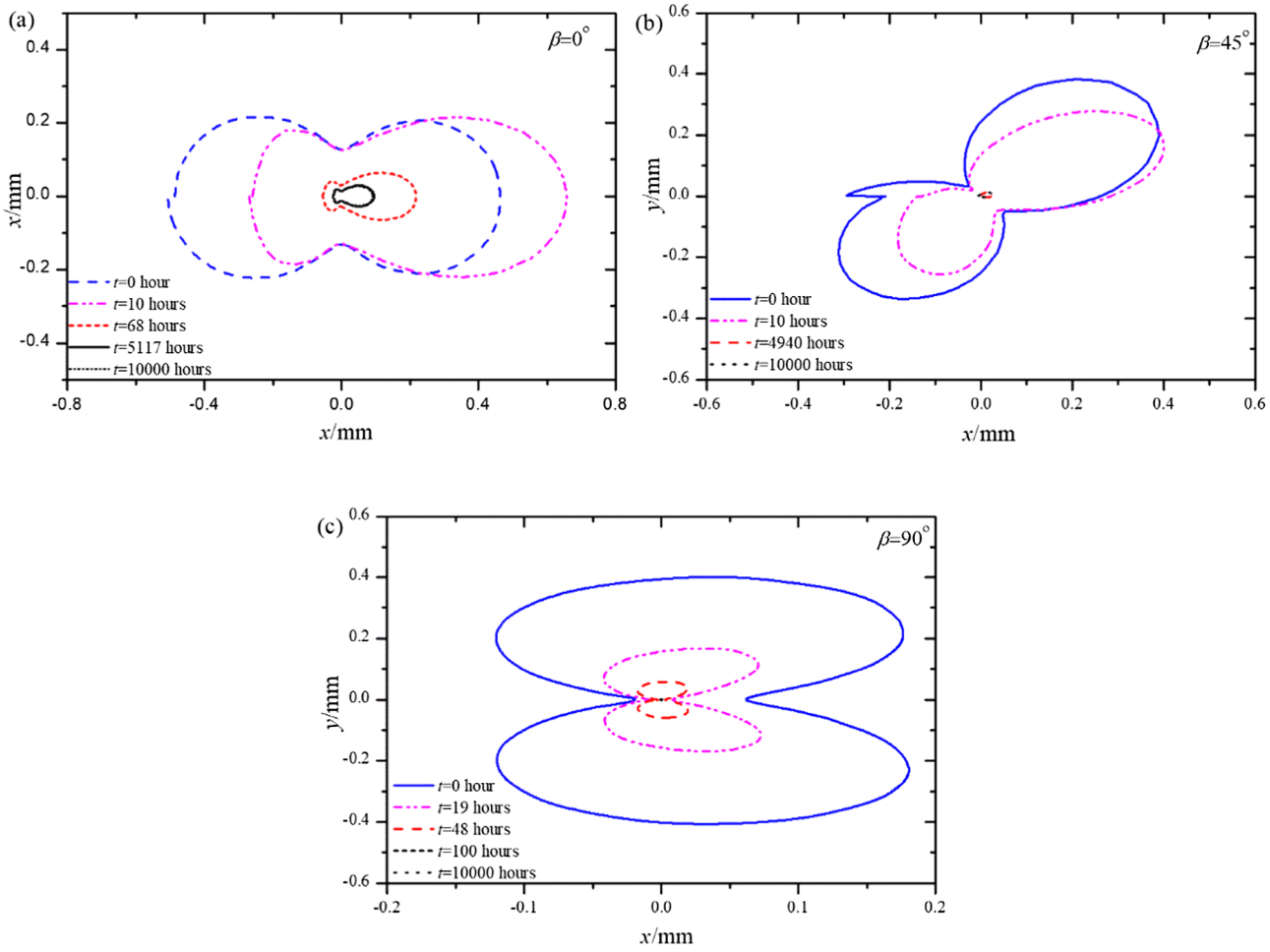

Fig. A2. Evolutions of equal equivalent stress with creep time for different shallow CTS specimens (a) $\beta = 0°$, (b) $\beta = 45°$, (c) $\beta = 90°$.

condition [12]. Under creep condition, the equal equivalent stress region decreases with the increase of creep time due to creep relaxation. The evolutions of equal equivalent stress region are also different from that of equivalent creep strain region as creep strain accumulates with the increase of creep time.

Appendix B. Supplementary material

Supplementary data to this article can be found online at https://doi.org/10.1016/j.tafmec.2020.102489.

References

[1] Y.W. Dai, Y.H. Liu, F. Qin, G.A. Qian, Y.J. Chao, C (t) dominance of the mixed I/II creep crack: Part I. Transient creep, Theor. Appl. Fract. Mech. 103 (2019) 102314.
[2] Y.W. Dai, Y.H. Liu, F. Qin, Y.J. Chao, H.F. Chen, Constraint modified time dependent failure assessment diagram (TDFAD) based on C(t)-A_2(t) theory for creep crack, Int. J. Mech. Sci. 165 (2020.) 105193.
[3] Y.W. Dai, Y.H. Liu, F. Qin, Y.J. Chao, F. Berto, Estimation of stress field for sharp V-notch in power-law creeping solids: an asymptotic viewpoint, Int. J. Solids Struct. 180–181 (2019) 189–204.
[4] Y.W. Dai, Y.H. Liu, F. Qin, Y.J. Chao, Notch stress intensity factor and C-integral evaluation for sharp V-notch in power-law creeping solids, Eng. Fract. Mech. 222 (2019) 106709.
[5] G.A. Qian, W.S. Lei, A statistical model of fatigue failure incorporating effects of specimen size and load amplitude on fatigue life, Phil. Mag. (2019) 1–37.
[6] G.A. Qian, W.S. Lei, L. Peng, Z. Yu, M. Niffenegger, Statistical assessment of notch toughness against cleavage fracture of ferritic steels, Fatigue Fract. Eng. Mater. Struct. 41 (5) (2018) 1120–1131.
[7] Y.J. Chao, X.K. Zhu, L. Zhang, Higher-order asymptotic crack-tip fields in a power-law creeping material, Int. J. Solids Struct. 38 (2001) 3853–3875.
[8] Y.W. Dai, Y.H. Liu, Y.J. Chao, Higher order asymptotic analysis of crack tip fields under mode II creeping conditions, Int. J. Solids Struct. 125 (2017) 89–107.
[9] Y.W. Dai, Y.H. Liu, F. Qin, Y.J. Chao, A unified method to solve higher order asymptotic crack-tip fields of mode I, mode II and mixed mode I/II crack in power-law creeping solids, Eng. Fract. Mech. 218 (2019) 106610.
[10] T. Keiichiro, I. Hitoshi, Elastic-plastic fracture toughness test under mixed mode I-II loading, Eng. Fract. Mech. 41 (1992) 529–540.
[11] V. Tvergaard, Effect of pure mode I, II or III loading or mode mixity on crack growth in a homogeneous solid, Int. J. Solids Struct. 47 (2010) 1611–1617.
[12] L. Stepanova, E. Yakovleva, Asymptotic stress field in the vicinity of a mixed-mode crack under plane stress conditions for a power-law hardening material, J. Mech. Mater. Struct. 10 (3) (2015) 367–393.
[13] S. Aoki, K. Kishimoto, T. Yoshida, M. Sakata, A finite element study of the near crack tip deformation of a ductile material under mixed mode loading, J. Mech. Phys. Solids 35 (1987) 431–455.
[14] H. Richard, K. Benitz, A loading device for the creation of mixed mode in fracture mechanics, Int. J. Fract. 22 (1983) R55–R58.
[15] S. Aoki, K. Kishimoto, T. Yoshida, M. Sakata, H. Richard, Elastic-plastic fracture behavior of an aluminum alloy under mixed mode loading, J. Mech. Phys. Solids 38 (1990) 195–213.
[16] M. Ayatollahi, M. Pavier, D. Smith, On mixed mode loading of a single edge notched specimen, Int. J. Fract. 82 (1996) R61–R66.
[17] T. Maccagno, J. Knott, The fracture behaviour of PMMA in mixed modes I and II, Eng. Fract. Mech. 34 (1989) 65–86.
[18] N. Choupani, Experimental and numerical investigation of the mixed-mode delamination in Arcan laminated specimens, Mater. Sci. Eng., A 478 (2008) 229–242.
[19] N. Hallbäck, The influence of finite geometry and material properties on mixed-mode I/II fracture of aluminium, Int. J. Fract. 87 (1997) 151–188.
[20] M.A. Sutton, A.P. Reynolds, J. Yan, B. Yang, N. Yuan, Microstructure and mixed

mode I/II fracture of AA2524-T351 base material and friction stir welds, Eng. Fract. Mech. 73 (2006) 391–407.
[21] M. Ayatollahi, M. Aliha, On determination of mode II fracture toughness using semi-circular bend specimen, Int. J. Solids Struct. 43 (2006) 5217–5227.
[22] M. Ayatollahi, M. Aliha, H. Saghafi, An improved semi-circular bend specimen for investigating mixed mode brittle fracture, Eng. Fract. Mech. 78 (2011) 110–123.
[23] N. Hallbäck, N. Jönsson, T-stress evaluations of mixed mode I/II fracture specimens and T-effects on mixed mode failure of aluminium, Int. J. Fract. 76 (1995) 141–168.
[24] M. Ayatollahi, M. Aliha, Analysis of a new specimen for mixed mode fracture tests on brittle materials, Eng. Fract. Mech. 76 (2009) 1563–1573.
[25] J. Brockenbrough, C. Shih, S. Suresh, Transient crack-tip fields for mixed-mode power law creep, Int. J. Fract. 49 (1991) 177–202.
[26] T. Hyde, A. Chambers, An experimental investigation of mixed-mode creep crack growth in Jethete M152 at 550 °C, Mater. High Temp. 9 (1991) 127–138.
[27] D. Poquillon, M. Cabrillat, A. Pineau, Mode II creep crack initiation in 316 LN stainless steel: experiments and modelling, Mater. High Temp. 16 (1999) 99–107.
[28] A.P. Gordon, D.L. McDowell, Mixed mode loading of an interface crack between graded creeping solids, J. Press. Vessel Technol. 126 (2004) 478–484.
[29] M. Kumar, I.V. Singh, B.K. Mishra, S. Ahmad, A.V. Rao, V. Kumar, Mixed mode crack growth in elasto-plastic-creeping solids using XFEM, Eng. Fract. Mech. 199 (2018) 489–517.
[30] L. Zhao, K.M. Nikbin, Characterizing high temperature crack growth behaviour under mixed environmental, creep and fatigue conditions, Mater. Sci. Eng., A 728 (2018) 102–114.
[31] F.H. Norton, The creep of steel at high temperatures, McGraw-Hill Book Company, Incorporated, 1929.
[32] J. Bassani, F. McClintock, Creep relaxation of stress around a crack tip, Int J Solids Struct 17 (5) (1981) 479–492.
[33] V.N. Shlyannikov, A.V. Tumanov, N.V. Boychenko, A creep stress intensity factor approach to creep–fatigue crack growth, Eng. Fract. Mech. 142 (2015) 201–219.
[34] Hibbitt, Karlsson, Sorensen, 2011. ABAQUS User's Manual, Version 6.10.
[35] G.Z. Wang, X.L. Liu, F.Z. Xuan, S.T. Tu, Effect of constraint induced by crack depth on creep crack-tip stress field in CT specimens, Int. J. Solids Struct. 47 (2010) 51–57.
[36] J.J. Han, Y.J. Kim, D. Jerng, K. Nikbin, D. Dean, Quantification of creep stresses within HAZ in welded branch junctions, Fatigue Fract. Eng. Mater. Struct. 38 (2015) 113–124.
[37] Y.J. Kim, J.-S. Kim, N.-S. Huh, Y.J. Kim, Engineering C-integral estimates for generalised creep behaviour and finite element validation, Int. J. Press. Vess. Pip. 79 (2002) 427–443.
[38] R. Ainsworth, P. Budden, Crack tip fields under non-steady creep conditions—I. Estimates of the amplitude of the fields, Fatigue Fract. Eng. Mater. Struct. 13 (1990) 263–276.
[39] M.F. Symington, C.F. Shih, M. Ortiz, Tables of Plane Strain Mixed-mode Plastic Crack tip Fields, Brown University Division of Engineering, 1988.
[40] V. Shlyannikov, A. Tumanov, Characterization of crack tip stress fields in test specimens using mode mixity parameters, Int. J. Fract. 185 (2014) 49–76.
[41] C.F. Shih, N. O'Dowd, M. Kirk, A Framework for Quantifying Crack Tip Constraint, Constraint effects in fracture, ASTM International, 1993.
[42] P.J. Budden, R.A. Ainsworth, The effect of constraint on creep fracture assessments, Int. J. Fract. 87 (2) (1997) 139.